Report for
80NSSC20M0261

Unmanned Aerial System (UAS) Research for Public Safety Applications

Task 1: Navigation and C2 Approaches to Degraded/Denied Environments
Final Report

Program Manager: Keenan Roach

Principal Investigator: Kenny Cheung

Prepared for

NASA Ames Research Center
Moffett Field, California
94035

Technical Report Documentation Page

Title: Task 1: Navigation & C2 Approaches to Degraded/Denied Environments

Report Date: April 30, 2024

Performing Organizations: University of North Dakota

Authors: Ryan Adams, Naima Kaabouch, Dalia Ammar Khodja, Kyle Foerster, Michael Mullins

Performing Organization and Address:
College of Engineering and Mines
University of North Dakota
Upson II Room 165
243 Centennial Dr Stop 8155
Grand Forks, ND 58202-8155

Sponsoring Agency Name and Address:
Universities Space Research Association
7178 Columbia Gateway Drive
Columbia, MD 21046

Table of Contents

Table of Figures

Table of Tables

Table of Acronyms

Acronym	Meaning
4G	Fourth Generation Communication System
ABT	Adaptive Belief Tree
AKF	Adaptive Kalman Filter
ASN	All Source Navigation
BVLOS	Beyond Visual Line-of-Sight
C2	Command and Control
CNN	Convolutional Neural Network
DEM	Digital Elevation Model
EKF	Extended Kalman Filter
ERP	Effective Radiated Power
FCC	Federal Communications Commission
F-CRLB	Filtering Cramer-Rao Lower Bound
FMCW	Frequency Modulated Continuous Wave
GIS	Geographic Information System
GPS	Global Positioning System
GUI	Graphical User Interface
HIFLD	Homeland Infrastructure Foundation-Level Data
IMU	Inertial Measurement Unit
INS	Inertial Navigation System
InSAR	Interferometric Synthetic Aperture RADAR
LeGO-LOAM	Lightweight and Ground-Optimized LiDAR Odometry and Mapping
LiDAR	Light Detection and Ranging
LIO-SAM	LiDAR Inertial Odometry via Smoothing and Mapping
LTE	Long-Term Evolution
MAV	Micro Air Vehicle
MAB	Multibranch Attention Module
POMDP	Partially Observable Markov Decision Process
RDA	Range Doppler Algorithm
RF	Radio Frequency
RGB	Red-Green-Blue
RGB-D	Red-Green-Blue Depth
RMS	Root Mean Square

RNN	Recurrent Neural Network
ROS	Robot Operating System
SAR	Synthetic Aperture RADAR
SLaM	Simultaneous Localization and Mapping
SN-MNN	Spectrally Normalized Memory Neuron Network
sUAS	Small Unmanned Aircraft System
SVM	Support Vector Machine
SVO	Semi-Direct Visual Odometry
SWaP	Size Weight and Power
TLE	Two Line Element
UA	Unmanned Aircraft
UAS	Unmanned Aircraft System
UBS	Ultrasonic Beacon System
UGV	Unmanned Ground Vehicle
UWB	Ultra-Wideband
VLOS	Visual Line-of-Sight
VO	Visual Odometry
VTOL	Vertical Takeoff and Landing
Wi-Fi	Wireless Fidelity

Executive Summary

The integration of Unmanned Aircraft Systems (UAS) into operational scenarios for first responders, particularly in rural or low population density areas, represents a significant advancement in rapid response and assessment capabilities. However, the effectiveness of these systems relies on robust Command and Control (C2) communications and reliable Global Positioning System (GPS) signals, which are crucial for operational safety and precise navigation. This project undertakes a comprehensive approach to document C2 communications (using the 4th Generation Long-Term Evolution communication system) and GPS navigation for UAS, focusing on three key areas: cellular coverage mapping, GPS signal quality assessment, and a review of the existing localization techniques in GPS denied environments.

1. **Cellular Coverage Mapping:**

The project's first objective is the development of a comprehensive map displaying cellular coverage from the four major service providers (Verizon, AT&T, US Cellular, and T-Mobile) across the 50 states of the USA, starting from ground level up to 400ft in receiver altitude. A modified version of the open-source RF Signal Propagation, Loss, and Terrain (SPLAT!) analysis tool was utilized, enhanced with multi-threading capabilities and high-resolution terrain data for accurate simulation. These simulations are meticulously compared against the FCC's 4G LTE coverage map, which serves as a benchmark, to ensure precision. By calibrating simulation parameters based on this comparison—adjusting the antenna height, ERP value, operating frequency, signal threshold, etc.—the project produces a detailed coverage map that helps operators identify regions with adequate service to maintain uninterrupted command and control capabilities for effective UAS deployment.

2. **GPS Signal Quality Mapping:**

The second component of the project involves creating a dynamically updating map of GPS signal quality across all 50 states. This map is particularly vital for navigation and precise positioning of UAS, especially in environments where GPS signals may be obstructed or weakened by geographical features. The GPS coverage map is generated using the latest satellite data (updated hourly) and accounts for terrain-induced signal blockage, providing a realistic overview of signal availability. This dynamic tool assists operators in real-time to adapt flight plans and operations according to the varying strengths of GPS signals across different regions.

3. **Review of Alternative Location Technologies:**

Recognizing the limitations of GPS in certain scenarios, the third focus of the project is a literature review on alternative technologies that can provide precise location information where GPS signals are inadequate. This review covers a range of emerging and established technologies, such as terrestrial-based technologies like LIDAR, and AI-based methods. The aim is to explore and evaluate these alternatives to supplement or replace GPS in scenarios where it fails to meet operational needs.

In summary, the research aims to fortify the foundational communication and navigational infrastructures required for effective deployment of UAS by first responders in challenging environments. By mapping cellular and GPS coverage and reviewing potential alternative technologies, the project supports safer, more reliable, and efficient UAS operations, thereby enhancing the capabilities of first responders in critical scenarios.

Introduction

Command, Control, and Navigation are critical functions for any Unmanned Aircraft System (UAS). These tasks become even more critical for first responders that operate in rural regions, or regions with low population density. Such scenarios can be significantly enabled by an accurate understanding of the coverage for command and control as well as the strength of Global Positioning System (GPS) signals in regions of prospective UAS flight. To assure reliable flight planning, particularly in rural areas of the country, this project combined three tasks: (1) develop a map to display cellular coverage for the major providers, (2) develop a dynamically changing map of GPS signal quality, and (3) perform a literature review of techniques that may be used to provide precision location information in regions with insufficient GPS signal strength.

4G LTE Coverage

Complex Factors Influencing Signal Propagation in UAS Communication Systems

In determining coverage for communication systems, especially for UAS, a range of environmental and technical factors can significantly impact signal effectiveness. While standard models typically focus on quantifiable elements like signal strength and terrain, other critical factors such as foliage, multipath interference, and the impact of building materials also play substantial roles, yet they are often not accounted for in primary analyses.

Foliage, for instance, contributes to signal attenuation through absorption and scattering of radio waves, especially in frequencies used by Long-Term Evolution (LTE) and other cellular communications. The density, type, and water content of vegetation can all influence signal reduction and coverage area. Similarly, multipath interference, arising from signal reflections from various surfaces like buildings and mountains, can lead to signal fading or connectivity loss, particularly in urban or complex topographic settings. Moreover, the construction materials of urban buildings can either absorb or reflect Radio Frequency (RF) signals, impacting signal propagation. Dense materials like concrete or brick can notably weaken RF signals, affecting coverage inside buildings and in their proximity.

These factors are omitted from the primary analyses in this work because of the complexity and variability they introduce into signal propagation models. Incorporation of elements like foliage density or specific building materials requires detailed, site-specific information that is difficult to obtain. Additionally, the dynamic nature of these factors, like seasonal changes in vegetation or urban development altering the existing environment, adds to the modeling challenge. Consequently, standard models usually prioritize more stable and measurable factors like terrain and signal strength, aiming for a balance between accuracy and practical applicability in coverage assessments.

In addition to these factors, the Doppler effect is another consideration. This phenomenon, observed when there is relative motion between the transmitter and the receiver, results in a change in the frequency of the received signal compared to the transmitted one.

When a UAS moves towards a transmitter, a positive Doppler shift is observed, meaning the observed frequency is higher than the transmitted frequency. Conversely, when moving away from the transmitter, the observed frequency decreases (negative Doppler shift). This shift can significantly impact communication system performance.

To see how fast a UAS would need to fly to experience a 1% shift in the carrier frequency, the Doppler effect formula for electromagnetic waves can be used:

$$f' = f * \left(\frac{c}{c \pm v}\right)$$

Where:

- f': is the observed frequency.
- f: is the transmitted frequency (carrier frequency).
- c: is the speed of light.
- v: is the velocity of the receiver relative to the source (the speed of the UAS).

For a 1% shift, f' would be either 1.01f or 0.99f, depending on whether the UAS is moving towards or away from the transmitter. Considering a carrier frequency of 2GHz, to experience a 1% increase in the carrier frequency due to the Doppler effect, a UAS would need to fly at an extremely high speed of approximately 3,030,303 m/s, or 10,909,090 km/h towards the source of the signal. This speed is extraordinarily high and far beyond the capabilities of any current UAS or aircraft. Such a Doppler shift is not feasible for UAS operations. This calculation highlights the fact that while the Doppler effect is a critical consideration in high-speed scenarios, such as in satellite communications or deep-space probes, its impact on UAS is negligible at typical operational speeds and is neglected for this analysis.

Comparative Analysis of Throughput Requirements in Manual and Automatic Unmanned Aircraft Modes

Upon a comparative analysis of Table 1 and Table 2, which present the estimated non-payload throughput requirements for a single Unmanned Aircraft (UA) in both manual and automatic modes, several insights emerge regarding communication demands during various flight phases.

In manual mode, as depicted in Table 1, the throughput requirements are notably higher across all communication links. This is particularly evident during the descent/landing phase, where the maximum throughput reaches 3,322 bytes/sec (or, 26,576 bits/sec). This peak value represents the worst-case scenario for throughput, demanding substantial data transmission to maintain control, navigation, and coordination. The heightened requirement is attributed to the pilot's need for increased data to manually manage the UA, coupled with the critical nature of the descent phase which necessitates heightened communication for safety and navigational precision.

On the other hand, Table 2 outlines a different profile for automatic mode operations. Here, the demand on the Command and Control (C2) link is significantly reduced, reflecting the UA's autonomous capabilities which require less intervention from the ground pilot. The most demanding phase in automatic mode shows a total throughput of 2,077 bytes/sec (or 16,616 bits/sec), substantially lower than its manual equivalent, emphasizing the efficiency of autonomous systems in reducing bandwidth requirements.

In essence, this analysis highlights the importance of communication systems capable of supporting the high data throughput required for manual UA operations, particularly during critical flight phases. The disparity between manual and automatic modes highlights the impact of autonomous systems on communication needs. Ensuring that communication systems are equipped to handle these peak demands is crucial for the operational integrity and safety of UA flights, with the worst-case scenario of 3,322 bytes/sec (or 26,576 bits/sec) in manual mode serving as a standard for system performance requirements.

Table 1: Estimated Non-Payload Throughput Requirements (bytes/sec) of a Single Unmanned Aircraft in Manual Mode. Data from [1].

Flight Phase	Forward / Return	C2 Link vs. Air/Gnd. RF Link	Aircraft Control	Aircraft Control + Navaids	ATC Voice Relay	Target Data	Total Throughput bytes/sec
Departure and Arrival (Takeoff/ Climbout)	Forward Link	C2 Link	115	188	600	N/A	903
		A/G Link	297	465	1144	N/A	1906
	Return Link	C2 Link	405	265	600	600	1870
		A/G Link	957	460	1144	695	3256
Transit/Extended Operations	Forward Link	C2 Link	N/A	199	600	N/A	799
		A/G Link	N/A	385	1144	N/A	1529
	Return Link	C2 Link	N/A	329	600	600	1529
		A/G Link	N/A	544	1144	695	2383
Departure and Arrival (Descent/ Landing)	Forward Link	C2 Link	390	276	600	N/A	1266
		A/G Link	946	476	1144	N/A	2566
	Return Link	C2 Link	420	312	600	600	1932
		A/G Link	973	510	1144	695	3322

Table 2: Estimated Non-Payload Throughput Requirements (bytes/sec) of a Single Unmanned Aircraft Operating in Automatic Mode. Data from [1].

Flight Phase	Forward / Return	C2 Link vs. Air/Gnd. RF Link	Aircraft Control	Aircraft Control + Navaids	ATC Voice Relay	Target Data	Total Throughput bytes/sec
Departure and Arrival (Takeoff/ Climbout)	Forward Link	C2 Link	N/A	79	600	N/A	679
		A/G Link	N/A	121	1144	N/A	1256
	Return Link	C2 Link	27	265	600	600	1492
		A/G Link	64	460	1144	695	2363
Transit/Extended Operations	Forward Link	C2 Link	N/A	47	600	N/A	647
		A/G Link	N/A	86	1144	N/A	1230
	Return Link	C2 Link	N/A	85	600	600	1285
		A/G Link	N/A	130	1144	695	1969
Departure and Arrival (Descent/ Landing)	Forward Link	C2 Link	81	88	600	N/A	769
		A/G Link	416	132	1144	N/A	1692
	Return Link	C2 Link	42	112	600	600	1354
		A/G Link	80	158	1144	695	2011

FCC Coverage Map

In the context of C2 communications for UAS, the correlation between LTE network coverage and the required data transmission rates is critical. The effectiveness of C2 communication relies heavily on consistent and reliable LTE coverage, underscored by the adoption of standard benchmarks such as 5 Mbps for uplink and 1 Mbps for downlink speeds. The data in Table 1 and Table 2 suggests that the required C2 throughput must exceed 3,322 bytes/second in order to support all activities of the UAS. In order to achieve reliable connection to the LTE network and to achieve sufficient throughput to effectively control a UAS, an additional margin is required. For this reason, the published benchmark of 5 Mbps for the uplink and 1 Mbps for the downlink is used throughout the document. The 5 Mbps uplink speed provides sufficient margin to transmit control signals and data from the UAS to the ground station, facilitating real-time operational control. Similarly, the 1 Mbps downlink speed provides ample throughput to receive operational commands and navigational data.

In this context, the Federal Communications Commission (FCC) Coverage map [2] shown in Figure 1, released on May 15, 2021, becomes a key resource. This map presents Fourth Generation (4G) LTE mobile broadband coverage across the United States and features separate layers for broadband and voice coverage from the nation's four largest mobile carriers: AT&T Mobility, T-Mobile, US Cellular, and Verizon Wireless. The data shown on this map, voluntarily submitted by these major carriers, provides the public with detailed information on mobile service coverage, as part of the broader Broadband Data Collection program. The criteria associated with this map, such as a 90% cell edge probability and 50% cell loading factor, with a maximum resolution of 100 meters for both voice and data coverage, aim to depict areas where users can expect minimum download speeds of 5 Mbps and upload speeds of 1 Mbps.

Utilizing the FCC Coverage map as a benchmark in this work allows for a comparative analysis to aid in evaluating the accuracy and reliability of data collection and the effectiveness of the technologies tested. By assuming a receiver position at ground level, the maps provide insights into the real-world applicability of LTE networks in supporting the requisite data rates for effective C2 communications in UAS operations. This analysis provides UAS operators with regions in which network connectivity satisfactorily meets the communication demands of each mission to ensure safe and efficient UAS deployments.

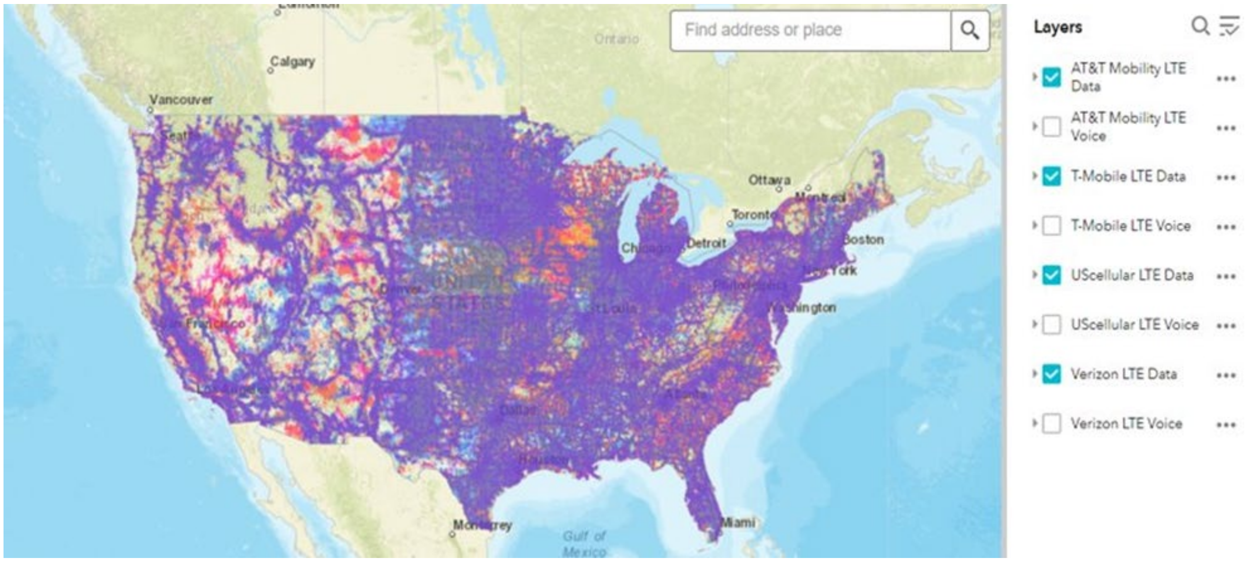

Figure 1: FCC map for 4G LTE coverage [2] as of May 15, 2021 (AT&T Mobility, T-Mobile, US Cellular, Verizon).

Available Data Sources

1.1.1 The Homeland Infrastructure Foundation-Level Data (HIFLD)

The Homeland Infrastructure Foundation-Level Data (HIIFLD) dataset [3] contains cellular tower locations as recorded by the FCC. This dataset is intended for use in Geographic Information Systems (GIS) for general planning, analysis, and research. The database contains a total of 2,4047 cellular locations. This number includes the four main operators (Verizon, AT&T, US Cellular, and T-Mobile) in addition to other independent providers.

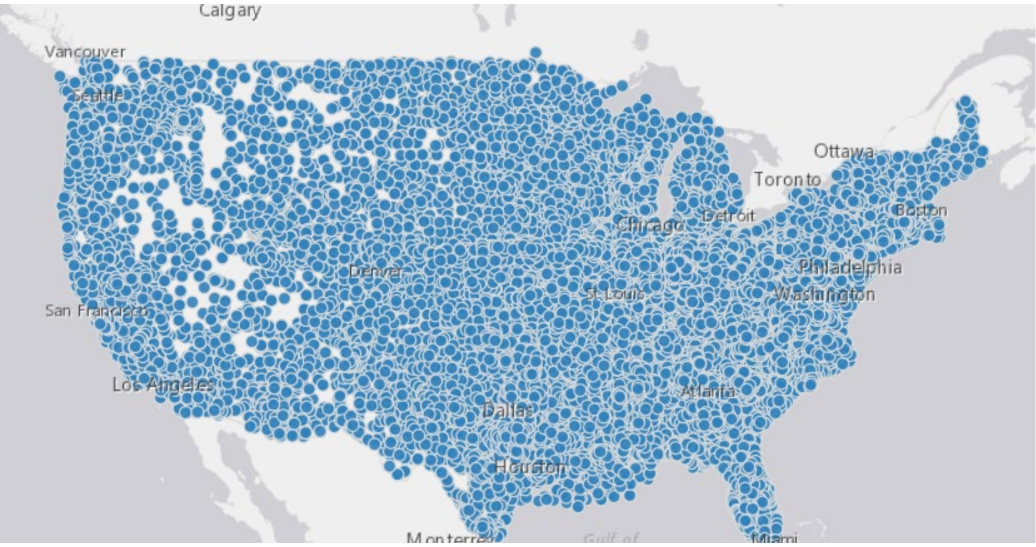

Figure 2: The Homeland Infrastructure Foundation-Level Data (all providers) from [3].

1.1.2 OpenCelliD

OpenCelliD [4] contains data that is primarily derived from smartphone users who use mobile applications such as OpenCelliD or OpenCelliD Client, and from commercial tracking devices such as black boxes. Additionally, corporations contribute through wholesale data donations. This collected data is then

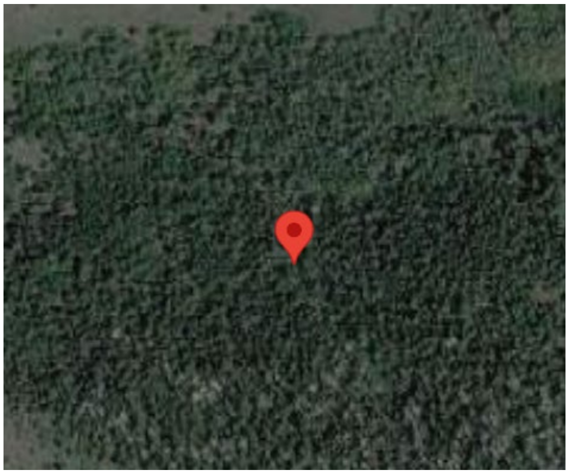

Figure 3: OpenCelliD [4] Example of Antenna Coordinates.

integrated into the OpenCellID API database. However, this dataset was excluded from use in this work because of its limited accuracy. The coordinates provided by the dataset incorporate an error margin that could extend up to 40 kilometers, making it unsuitable for the specific needs of this project. Figure 3 illustrates a cellular tower's location as indicated by OpenCelliD, highlighting the absence of an actual tower at that specific location. The dataset indicates that the actual position of the cellular tower could potentially be located anywhere within an estimated 37km radius from the given coordinates as shown in Figure 4.

Figure 4: OpenCelliD [4] Position Error Margin.

1.1.3 US Cellular Tower Locator

The US Cellular Tower Website [5] provides US Cellular tower locations.

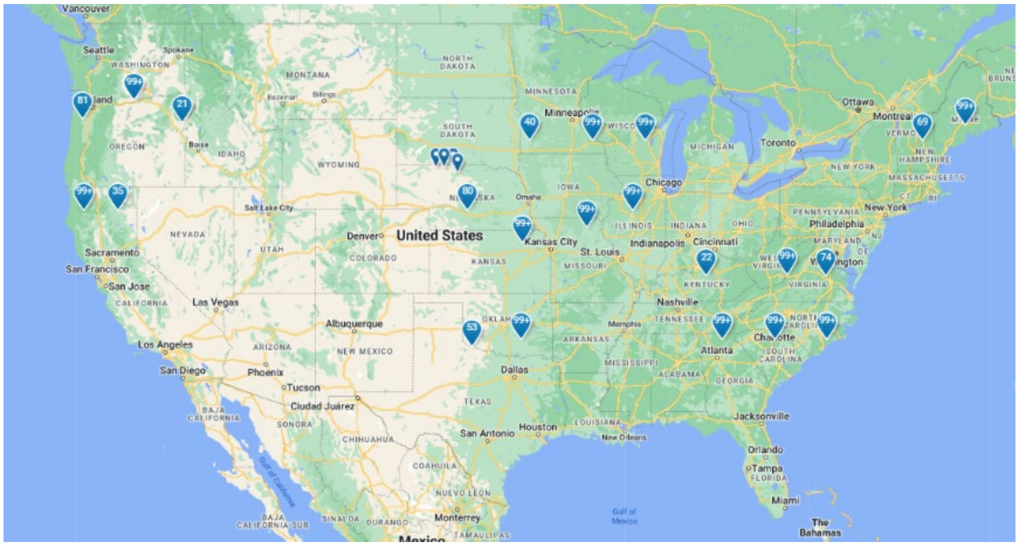

Figure 5: US Cellular Tower Locator Data [5].

Additional Data Collection

Due to the incompleteness of the datasets provided by the previous sources, extensive additional data was gathered using three main approaches:

1.1.4 Cellmapper

Cellmapper [6] utilizes crowd-sourced data, gathered from a broad user base, to provide cellular tower locations as shown in Figure 6. For added precision, the data is cross verified with Google Maps, enhancing the accuracy of the tower location information.

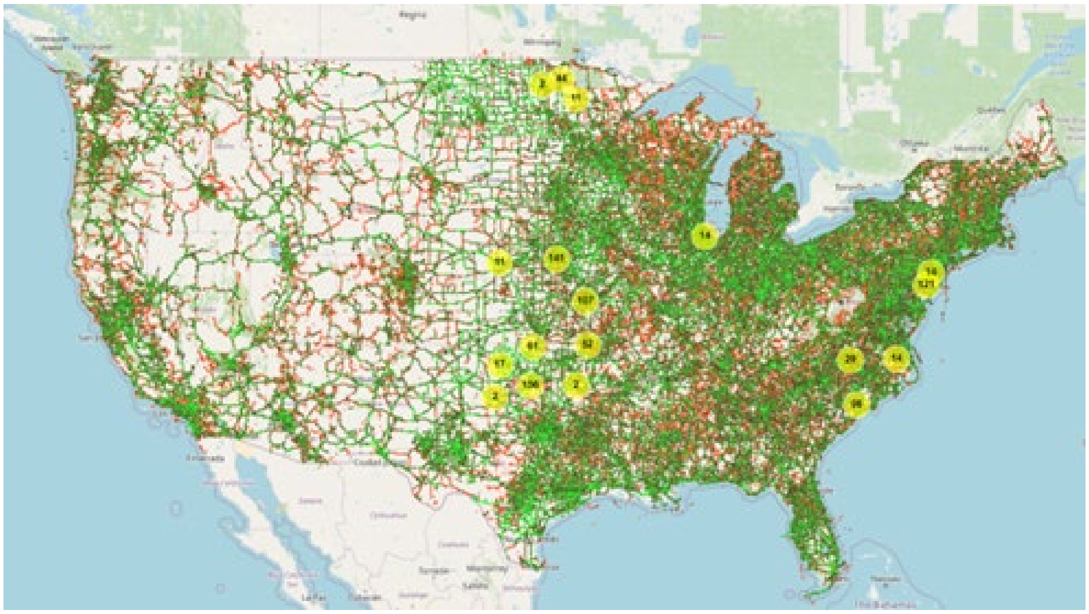

Figure 6: Cellmapper Crowd-Sourced Data [6].

1.1.5 Botlink-Developed Web Tool

Additional data was collected from the Botlink-Developed Web Tool. This involved zooming into the website's maps to identify clear antenna patterns indicating tower locations as shown in Figure 7, followed by extracting the precise coordinates of these towers.

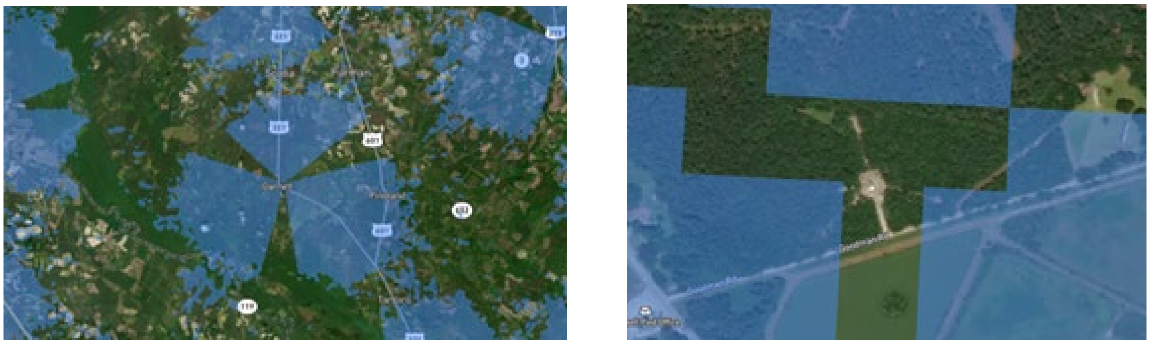

Figure 7: Extraction of Tower Locations Using Botlink-Developed Website.

1.1.6 AntennaSearch

AntennaSearch [7] offers information on a variety of towers, including the cellular ones. As shown in Figure 8, the website provides all the antennas and towers within a 3-mile radius of the input coordinates. However, it requires manual filtering to extract data specifically related to cellular towers and then to the four main providers, given the broad range of tower types listed.

From the combined data sources of Cellmapper, Botlink Website, and AntennaSearch, a total of 14,946 cellular tower locations were identified, recorded and added to the available datasets.

Figure 8: AntennaSearch [7] Data Example.

LTE Coverage Simulation

The simulation process began by leveraging the existing data contained in the HIFLD and US Cellular tower locator datasets. This approach, however, resulted in incomplete coverage with notable gaps caused by a significant number of missing antenna locations as depicted in Figure 10 and Figure 9. To address this inadequate set of antenna locations, a data acquisition phase was undertaken during which tower locations were collected from sources described above including Cellmapper, AntennaSearch, and the Botlink website. Upon integrating the additional identified antenna locations, updated simulation outcomes were cross-referenced with the FCC coverage maps. Differences identified during this comparison were resolved through adjustments to the simulation parameters to improve alignment with the reported FCC coverage.

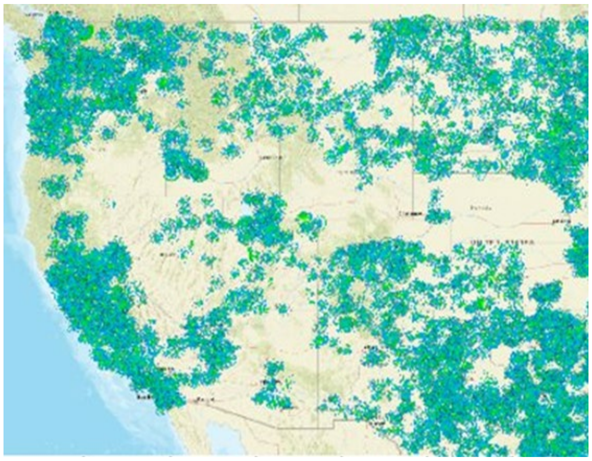

Figure 10: Initial Simulation Result for AT&T Operator over the Western Half of the Continental USA.

Figure 9: Result for the AT&T Operator for the Western Half of the Continental USA.

1.1.7 LTE COVERAGE ANALYSIS

The type of communication used for C2 of UAS varies depending on the type of UAS, planned operational parameters, and the type of environment the UAS will be flying in. The two most common divisions for type of operation are visual line-of-sight (VLOS) and beyond visual line-of-sight (BVLOS). In the case of VLOS operations, C2 is usually accomplished using direct communication methods such as radio transmitters, wireless fidelity (Wi-Fi), or Bluetooth receivers. For BVLOS operation, reliable long-range communication methods are used, such as LTE communications, to extend operational range well beyond common radio limits.

To support UAS operations in both VLOS and BVLOS scenarios, analysis of LTE coverage can accelerate the planning process to determine the feasibility of operations for a given area using LTE as a mechanism for C2 communications. For this C2 method the FCC provides a coverage map for LTE data derived from data provided by the major LTE providers in the United States that meets a defined set of performance requirements, such as 5Mbps down and 1Mbps up. [2] These throughput requirements meet the required minimum rates for C2 communication, as discussed in Section 0.

Specifics on how these coverage maps were generated are not provided by the FCC and may not be consistent between each provider. To validate these coverage maps and generate a non-provider version of the coverage map, an analysis of LTE coverage was performed for the four major cellular providers in the United States: Verizon, AT&T, T-Mobile, and US Cellular using a UND developed simulation tool.

1.1.8 Simulation Tool

The coverage analysis was performed using a modified version of an open-source RF Signal Propagation, Loss, and Terrain analysis tool SPLAT!. [8] This tool provides an easy-to-use method to simulate RF propagation including the effects of path loss and terrain blockage.

The modified version of the tool supports additional features such as multi-threading computation to accelerate simulation time as compared to the single threaded version of SPLAT!. Support for higher resolution terrain data, such as Light Detection and Ranging (LiDAR) data, and basic radiation pattern profiles are supported in horizontal and vertical directions.

The modified tool also includes a Graphical User Interface (GUI) and command line wrapper to allow for easier use of the tool and automation of command line parameters and identification of the correct terrain to use for the tool to provide accurate results. The GUI interface for the tool is shown in Figure 11.

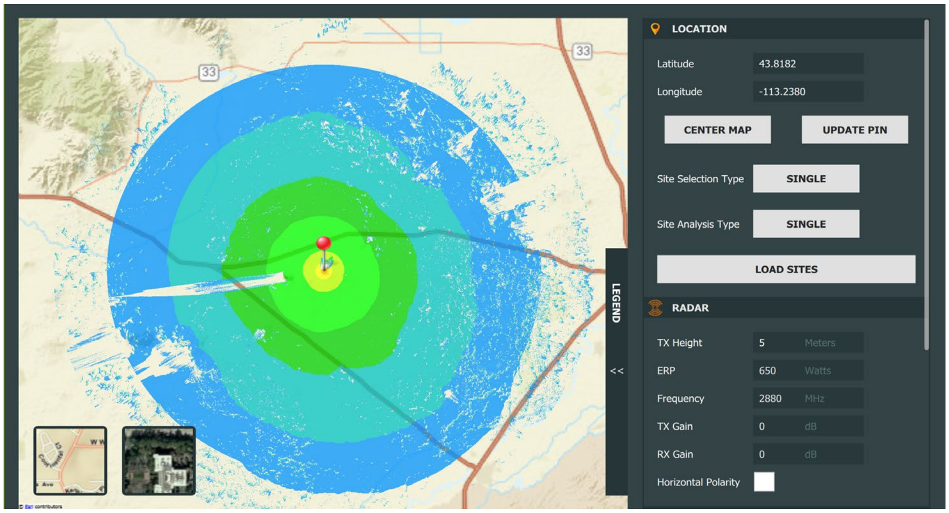

Latitude 43.8182
Longitude -113.2380
Site Selection Type SINGLE
Site Analysis Type SINGLE
TX Height 5 Meters
ERP 650 Watts
Frequency 2880 MHz
TX Gain 0 dB
RX Gain 0 dB
Horizontal Polarity ☐

Figure 11: GUI Wrapper for RF Analysis Tool.

1.1.9 Initial test results

To provide timely analysis results and ensure the resulting dataset is a reasonable size, the analysis was performed using 3-arcsecond (~90m) terrain data and the underlying tool was configured to use ITWOM 3.0 for the path loss calculation since it should provide high quality results in areas near transmitters.

Before beginning the full analysis, multiple test sites that had most of their parameters and configurations defined were chosen and simulated to verify the tool would produce results that are valid for a given LTE antenna location. The first test site results are shown below in Figure 12 for a US cellular site in Northern California where the results are relatively similar with gaps in the same relative locations around the tower. Similar coverage patterns can be seen on the south facing sides of the mountains in the top left corners of

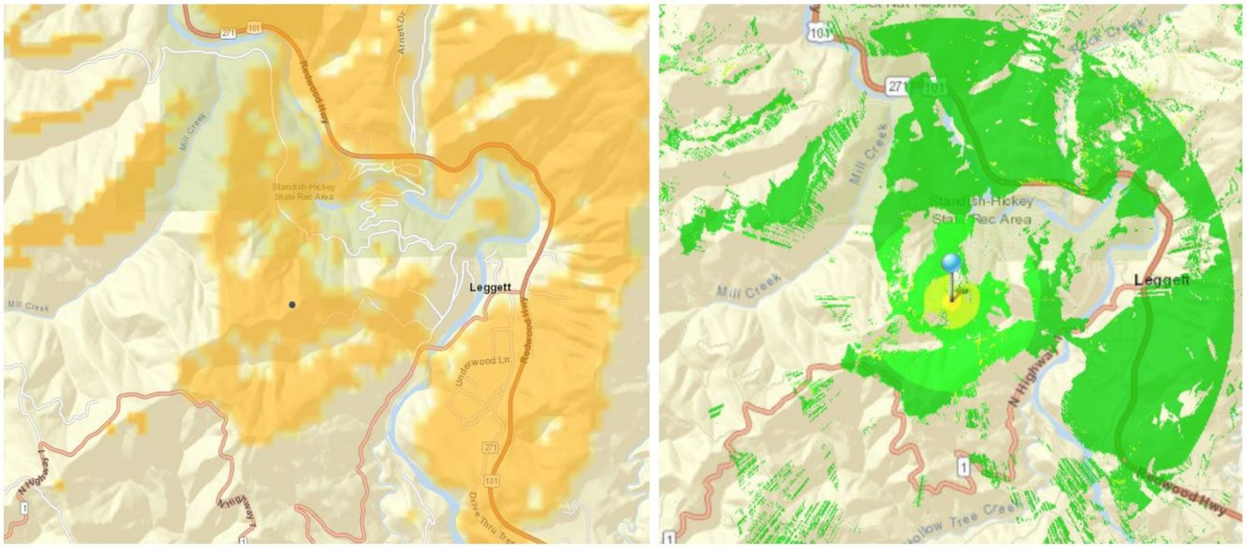

Figure 12: LTE Analysis Test Site #1, FCC (left) and Tool (right).

the images and the same gaps from valleys and blockage from mountains can be seen between the coverage maps from the providers and the results generated by the analysis tool.

The results for a second site US Cellular site are shown in Figure 13, where again, the results are relatively similar with gaps in the same areas with large gaps produced by the mountain in the same relative areas. The tool did indicate better coverage at the edges but this is most likely from not using the exact same configuration and analysis tool as the cellular provider.

Figure 13: LTE Analysis Test Site #2, FCC (left) and Tool (right).

1.1.10 Simulation Parameters

Simulation of LTE coverage involves several parameters that can significantly influence the accuracy of the result. Key parameters used by the BPANE simulation tool include the following:

- **Antenna Height**: This is the height of the cellular antenna above the ground. This critical parameter has a significant impact on range and signal quality because of the need for line-of-sight communication with the receiver. Antennas that are located at higher elevations exhibit fewer problems associated with obstacles on the ground. The HIFLD dataset specifies only the maximum elevation of the entire structure, not the height of the antenna itself. For simulation purposes, it is assumed that the antenna is mounted at a point which is 75% to 80% of the maximum height of the structure.
- **Effective Radiated Power (ERP)**: This parameter represents the power radiated by the antenna to the surrounding area. ERP is calculated by combining the power output from the transmitter and the gain of the antenna. The value of ERP strongly influences the effective range of signal propagation. In the HIFLD dataset, the Effective Radiated Power for approximately 84.5% of the antennas is recorded to be 140.82 Watts.
- **Receiver Height**: The height of the receiver above the ground also affects signal reception. Receivers at higher elevations experience fewer obstructions and potentially better signal quality at the receiver. The receiver height shown in the FCC coverage maps of [2] is assumed to be at

ground level to compare with simulations performed at ground level. Additional simulations were performed at 50ft steps up to a maximum height of 400ft above ground level.

- **Operating Frequency**: The operating frequency also has a strong effect on signal propagation and penetration through materials. The FCC Universal Licensing System website provided details about the frequencies used by the licensees as shown in Figure 14.

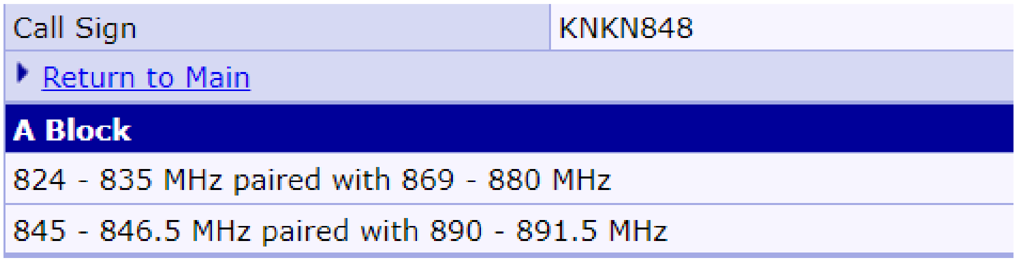

Call Sign	KNKN848
Return to Main	
A Block	
824 - 835 MHz paired with 869 - 880 MHz	
845 - 846.5 MHz paired with 890 - 891.5 MHz	

Figure 14: FCC Universal Licensing System Website Data on Operator Frequencies [181].

- **Range Limit:** This parameter defines the maximum radius of the simulation from the transmitter, measured in either kilometers or miles. This distance sets the outer boundary of analysis for the coverage area of each cell location for each operator. For each cellular antenna, a range of 30km was set for the Verizon network, while a larger range limit of 40km was applied for US Cellular, AT&T, and T-Mobile.
- **Signal Threshold:** The simulation display incorporates a minimum threshold expressed in dBm or dBuV/m. Any signal value below this threshold will not be displayed in the resulting image. The values used in the simulation varied in the range of –86dBm to –73dBm.
- **Terrain Resolution:** The simulation employed a terrain resolution of 3 arcseconds.

1.1.11 Parameter Tuning

During the course of simulations, key parameters such as antenna height, signal threshold, and antenna range were tuned and adjusted after comparison to the FCC coverage map.

In instances where the antenna height was not explicitly specified, particularly with respect to the data collected, an approach was adopted where nearby antenna heights were examined and a similar height was

Figure 15: Simulation Results with a 70dBm Signal Threshold.

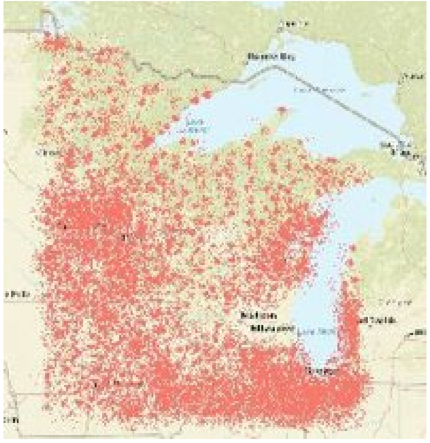

Figure 16: Simulation Results with a 75dBm Signal Threshold.

assumed for the simulation. This method provided a basis for initial estimations. Subsequent to this, if the simulation results indicated an under coverage or an over coverage, adjustments were made to the signal threshold to better align the results with expected coverage patterns. Figure 15, Figure 16, Figure 17, and Figure 18 illustrate the impact of modifying the signal threshold on the simulation outcomes.

Figure 17: Simulation Results with a 81dBm Signal Threshold.

Figure 18: Simulation results with a 86dBm Signal Threshold.

The range limit parameter was considered as a secondary adjustment strategy. This parameter was particularly relevant in cases where modifications to antenna height and signal threshold alone were insufficient to achieve an accurate representation of coverage. An illustrative example of this optimization step can be seen with the Verizon operator's data, where an initial over-coverage was observed. Despite attempts to rectify this erroneous result through reductions in antenna height and signal threshold, the desired coverage was not attained. Consequently, a reduction in the range limit from 40 kilometers to 30 kilometers was implemented with positive results achieved.

Simulation Results

1.1.12 US Cellular Operator

The simulation process began with the US Cellular operator, chosen specifically because it has the smallest network of towers in the United States. Data from the US Cellular locator website and the FCC Coverage map reveals that the coverage provided by this operator is restricted to a limited number of states.

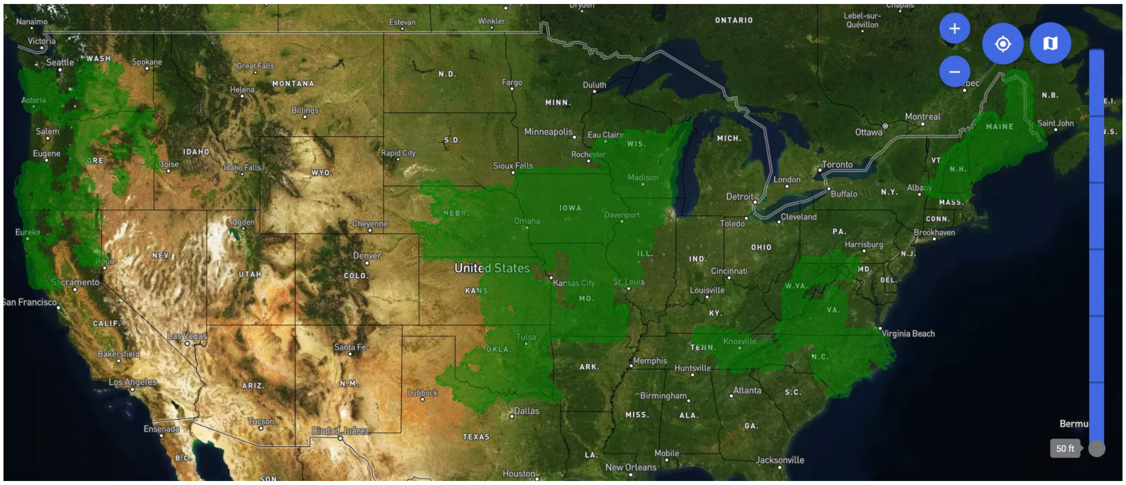

Figure 20: Coverage Simulation Results for US Cellular Operator with a 50ft Receiver Height.

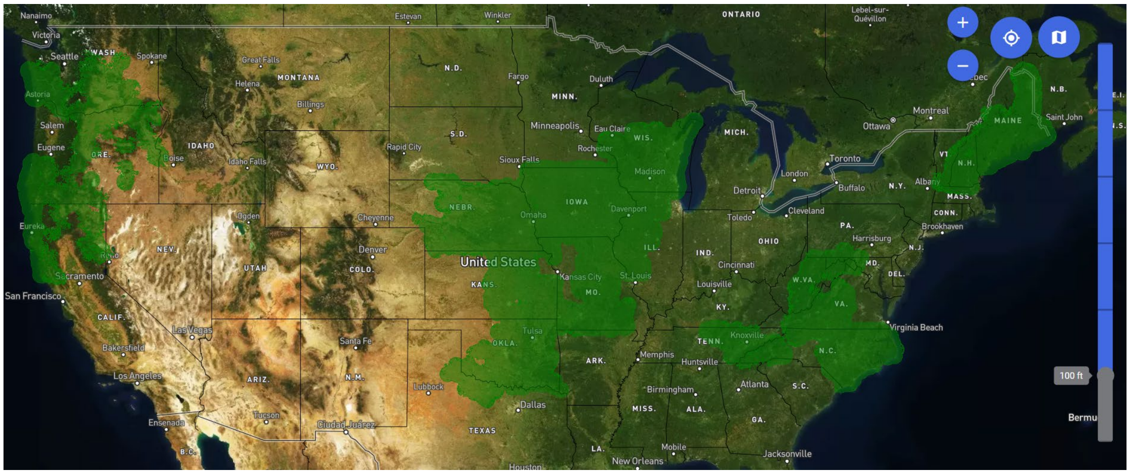

Figure 19: Coverage Simulation Results for US Cellular Operator with a 100ft Receiver Height.

The simulation parameters were tuned to align with actual network characteristics. The range limit was set at 40km to represent the maximum effective communication radius from each cellular tower. In determining antenna height, an average of 50m was calculated based on the available data for the collected tower locations. Additionally, the ERP was set at an average of 140 Watts. Upon establishing the aforementioned parameters, the signal threshold was tuned, with each resulting simulation outcome being compared against the FCC coverage map. The process began with an initial signal threshold of -86dBm, which, upon analysis, indicated over coverage. Subsequently, the threshold was adjusted until it reached the value of -76dBm for the majority of antennas, and -70dBm for some regions where the coverage was limited.

The simulation results for this operator are shown in Figure 20, Figure 19, and Figure 21. These figures demonstrate that coverage improves with increased receiver height, with no noticeable change in coverage after the receiver height reaches 100ft.

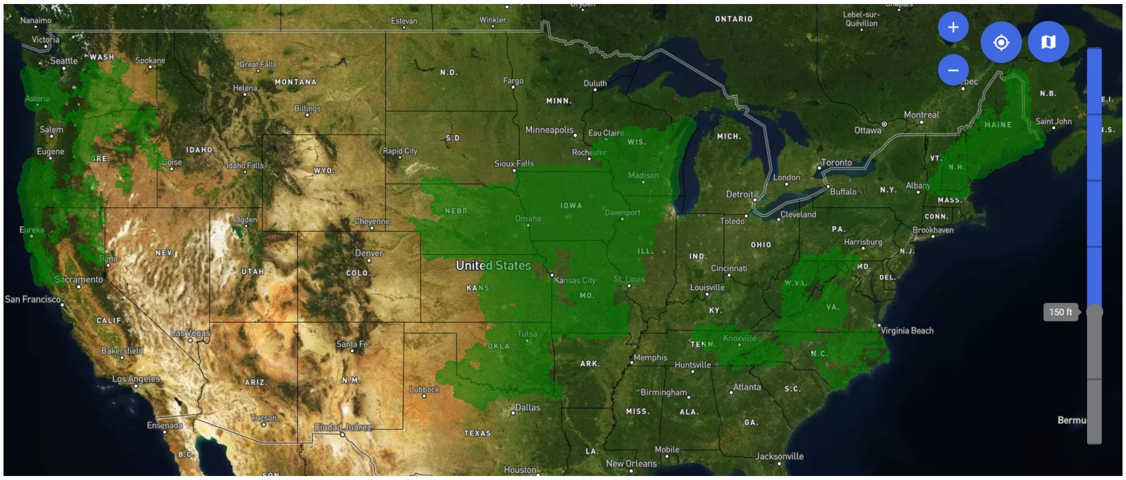

Figure 21: Coverage Simulation Results for US Cellular Operator with a 150ft Receiver Height.

1.1.13 Verizon Operator

Adopting a similar approach to the one used previously, the initial parameters for the simulations included a 40km range limit and an antenna height determined by averaging the heights from the collected location data near the desired antenna. The ERP was also set at an average of 140 Watts. However, initial simulations with these settings indicated over coverage. Adjustments to the antenna height and ERP value were made in an attempt to rectify this erroneous result, but these modifications did not yield the expected results. Consequently, it became necessary to decrease the range limit for this operator from 40km to 30km to achieve a more accurate depiction of coverage.

1.1.14 AT&T Operator

For the AT&T operator, the simulation followed a methodology similar to the one used previously. The range limit was established at 40km, and the signal threshold was carefully adjusted. This process resulted in a range of threshold values, varying from -86dBm to -76dBm, depending on the specific region within the country being analyzed.

1.1.15 T-Mobile Operator

The T-Mobile operator presented the most challenges in the simulations. Within the HIFLD dataset, there were only 59 cellular tower locations for T-Mobile, necessitating extensive data collection to bring the total up to 11,895 locations. The simulation process was divided based on geographical location, focusing separately on the western and eastern sides of the country. For each region, the simulation parameters experienced multiple rounds of adjustment to align closely with the coverage depicted in the FCC coverage map. The signal threshold values varied significantly, with most locations on the western side using around -86dBm, while on the eastern side, thresholds were adjusted to -70dBm, -73dBm and -74dBm depending on the coverage. The average estimated antenna height was set to 50 meters, and a uniform range limit of 40 kilometers was applied for all cellular antenna locations on the T-Mobile network.

Examples

1.1.16 Scenario 1: Hiker in the Brownlee Reservoir Region on the Idaho/Oregon Border

In the context of search and rescue operations within the Brownlee Reservoir region, characterized by its rugged terrain, the variability and inconsistency of LTE signal coverage presents a significant challenge as shown in Figure 22 for the Verizon operator. The search pattern must consider the zones where signal is absent, ensuring that search teams can communicate effectively despite the presence of regions of inconsistent coverage. Additionally, it is crucial to consider the receiver elevation, as the coverage improves at higher altitudes.

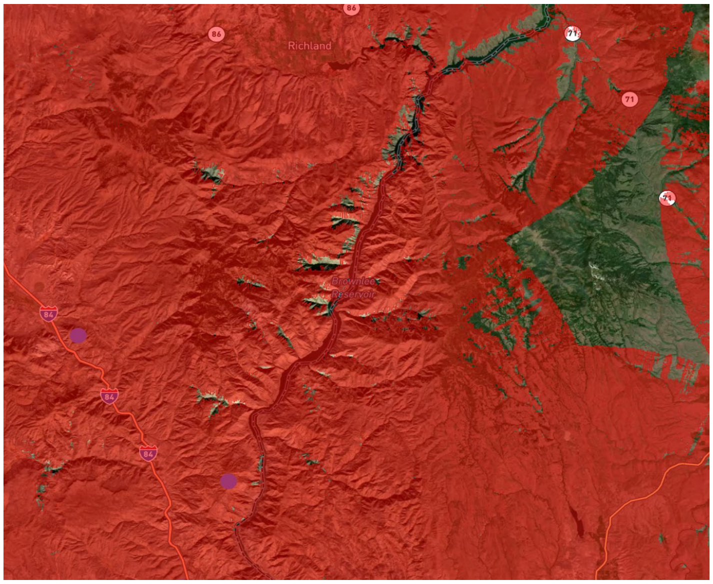

Figure 22: Verizon Coverage in the Region of Brownlee Reservoir on the Idaho/Oregon border with a Receiver Height of 400ft.

1.1.17 Scenario 2: Wildfire Discovered in the Northeast Region of Durango, Colorado

In the event of a wildfire northeast of Durango, Colorado, the assessment of the fire's extent is complicated by the area's uneven and rugged terrain. As depicted in Figure 23, LTE coverage is inconsistent, with noticeable differences between Verizon (indicated in red) and AT&T (indicated in blue). To determine the wildfire's size with precision, a flight plan (highlighted in yellow) has been developed. This plan considers these factors to ensure that the fire is monitored effectively despite the uneven signal availability.

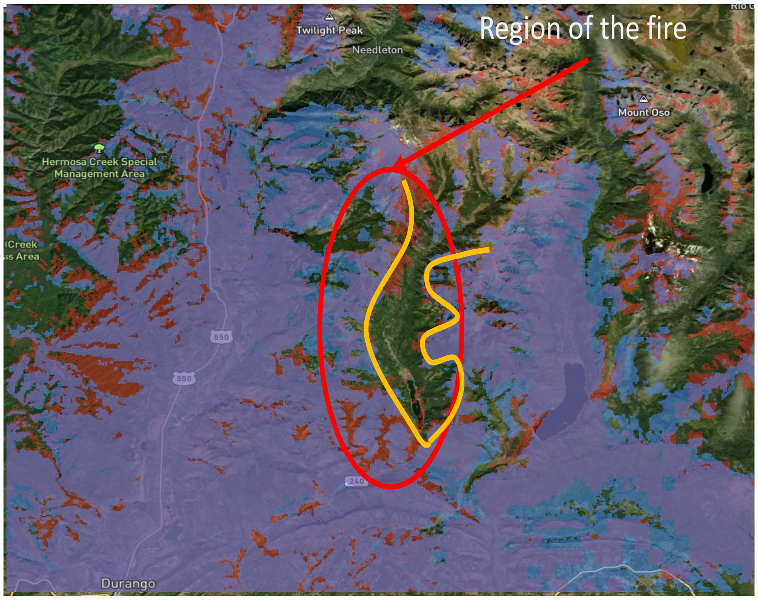

Figure 23: Scenario of a Fire in the Region Northeast of Durango, Colorado.

1.1.18 Scenario 3: Avalanche Occurrence in the Mountainous Region of the Sierra Nevada

Similarly, the consequences of an avalanche require a detailed evaluation of the affected area. For example, in the Sierra Nevada mountains, the terrain's steep and complex nature significantly affects the reliability of LTE signals, as shown in Figure 25, with the coverage for Verizon operator. Search and recovery strategies must be adapted to these communication dead zones, ensuring that rescue teams maintain coordination in the absence of stable connectivity. The effectiveness of search and recovery efforts in the extent of an avalanche can be significantly enhanced if the receiver is positioned at a higher altitude. In the case of the Sierra Nevada mountains, elevating the receiver to 400ft markedly improves communication coverage, as illustrated in Figure 24. This increase in altitude leads to better signal reception compared to a lower altitude of 50ft, thereby facilitating a more accurate and efficient evaluation of the area.

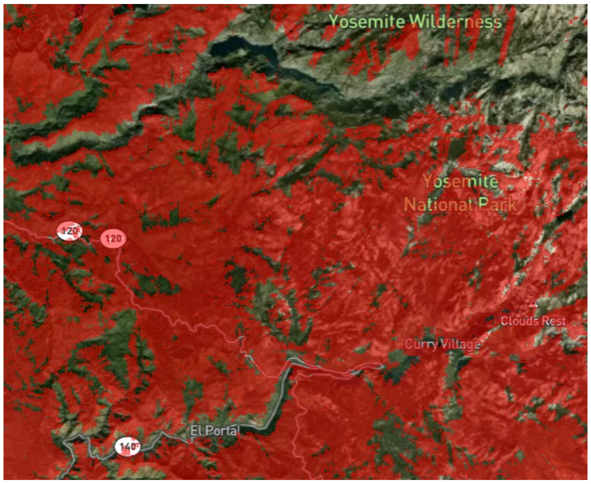

Figure 25: Scenario of an Avalanche in the Mountainous Region of Sierra Nevada (Coverage at 50ft receiver height).

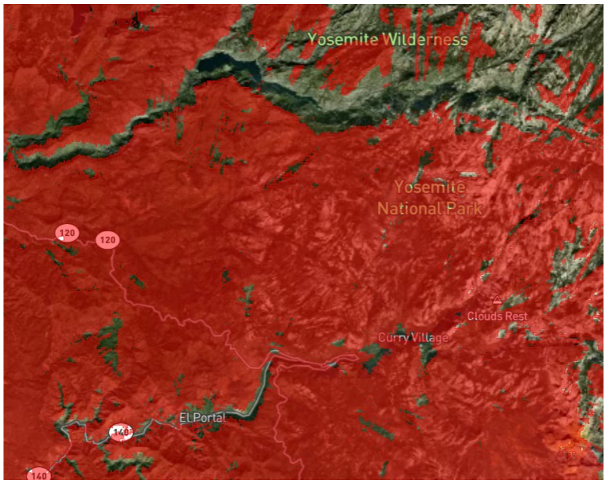

Figure 24: Scenario of an Avalanche in the Mountainous Region of Sierra Nevada (Coverage at 400ft receiver height).

GPS Coverage Analysis

The Global Positioning System (GPS) is a vital service that is required for normal operation of most UAS, especially small UAS. For the case of small UAS, GPS may be the only primary positional sensor available and depending on the type of operation being performed by the UAS, may be critical to its safe operation. When the UAS is operating in close proximity to structures or performing semi-automated tasks like linear infrastructure inspection, high accuracy GPS information is needed to maintain safe distances but also stay within range of the structure or object being inspected. Another use-case is during emergency operations, like forest fire fighting, the UAS may be operating in mountainous areas that may have blind spots for GPS coverage due to the terrain features.

To help support the operation of UAS, especially small UAS (sUAS), in these types of environments, analysis of GPS coverage will be useful. This type of analysis can be used to speed up the process of planning operations for an area and to help reduce the potential for loss of GPS signal during operations. With this goal in mind, the project developed a GPS coverage analysis map for UAS operations within the United States of America. This map is meant to provide reasonably accurate and up to date GPS coverage analysis using the current orbital position information of GPS satellites while also taking terrain blockage into account when generating the coverage map. The current coverage analysis does not include obstacle or structure information, just terrain information.

The generation of the GPS coverage map involves four main steps. The first is pulling the latest GPS satellite orbit information, projecting it to the current time, and converting it to the same reference frame as the rest of the calculations. The second step involves calculating the number of visible satellites with terrain blockage for the entire analysis area of the United States of America. The third step involves converting the visible satellite counts into a visible map layer for the GUI interface developed by Botlink that displays gaps in coverage based on a user defined number of required satellites.

Since terrain data does not normally change significantly and to help speed up the coverage analysis, the terrain line-of-sight blockage was precalculated using a uniform grid that the rest of the coverage analysis steps use. This approach allows the coverage analysis program to look up the elevation angle (line-of-sight) for the current location without having to perform a full path analysis between the current location and the current position of every GPS satellite every time the coverage analysis is updated.

Terrain Data and Reference Grid

All of the stages of the coverage analysis use the same reference terrain dataset and grid system based on the reference system used by the 3-arcsecond (~90m) terrain data. This grid spacing was chosen to reduce the overall size of the generated data sets and to keep the processing time low enough to allow for updating the coverage analysis every hour. The terrain data itself is divided into 1-degree by 1-degree latitude/longitude squares with each 3-arcsecond terrain file containing 1,201 x 1,201 grid points evenly distributed over the 1x1 degree area. This terrain reference system is used by the GPS coverage analysis program and all of the output files from the analysis tools are broken up into the same 1x1 degree areas with the same number of grid points within each file.

The coverage analysis is performed over the land area of the United States of America which encompasses 1410 1x1 degree areas, each with 1,442,401 grid points for a total of a little over 2 billion grid points for the United States. The main areas covered are the Continental United States, Alaska, Hawaii, and Puerto Rico, as shown in Figure 26.

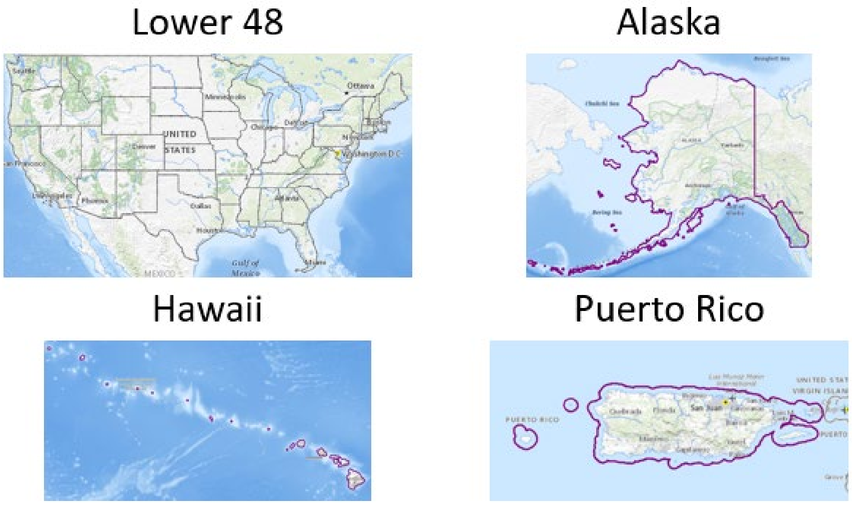

Figure 26: GPS Analysis Coverage Area.

Three different sets of terrain data at varying resolutions were pulled from two publicly available sources, USGS [9] and EarthExplorer [10]. The three terrain resolutions used by the coverage analysis program, during development of the tool, and for the generation of the datasets are 1/3-arcsecond (~10m), 1-arcsecond (~30m), and 3-arcsecond (~90m) terrain elevation data.

GPS Positional Data Source

The up-to-date GPS position information is obtained by downloading current Two-Line Element (TLE) orbit predictions for the GPS satellites from Space-Track [11]. During development and testing of the tools and web interface, Celestrak [12] was used instead since it is free and does not require an account for usage.

The GPS TLE orbit information is then processed into a more usable format for calculation purposes using an open-source python library called Skyfield. [13] This library allows calculation of orbit information for celestial bodies and, for our purposes, is used to calculate the current GPS satellite position by projecting the TLE orbit prediction forward in time and then converting its current location into the same reference frame as the grid points and terrain data, WGS-84.

Terrain Line-of-Sight Pre-Calculation

Since the terrain data does not normally change over time and all of the tools and programs developed for this project use the same reference grid as the 3-arcsecond terrain data, the terrain line-of-sight calculation only needs to be performed once and the results of this analysis can be used as a look up dataset to significantly speed up calculation. This dataset contains the geodetic elevation angle for a given heading at the current gird point as shown in Figure 27.

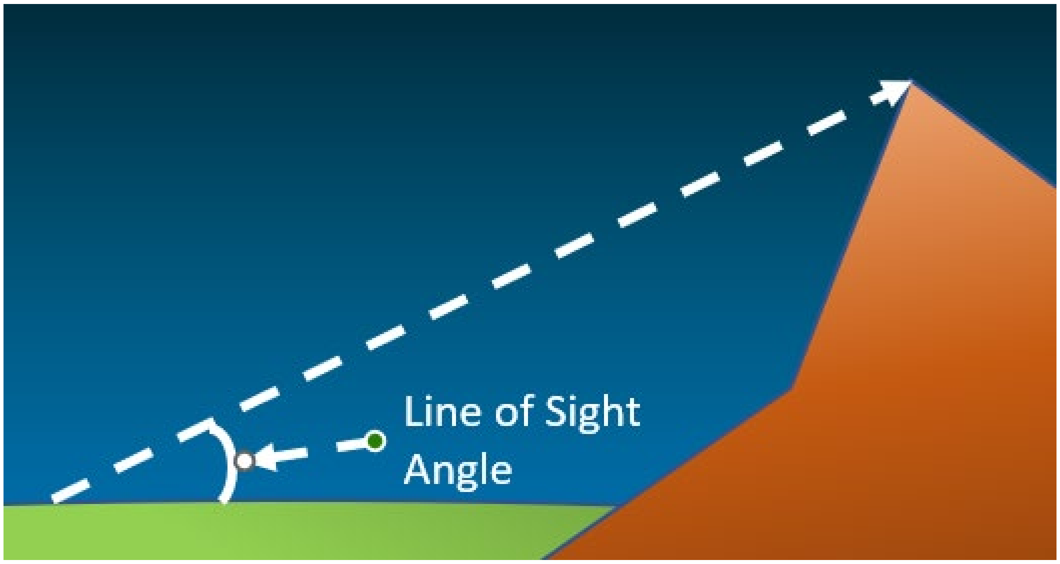

Figure 27: Precalculated Terrain Line-of-Sight.

The precalculated terrain line-of-sight data uses the same reference grid as the rest of the program with the line-of-sight calculation for each grid point being performed at a 1-degree heading increment for a total of 360-degrees of line-of-sight data for each of the grid points and an overall total of about 732 billion line-of-sight angles for the entire United States of America.

The process of generating this data set consisted of iterating over every grid point and calculating line-of-sight for each of the 360 headings, each tracing a path at the desired heading and calculating the largest line-of-sight angle on the path. The path calculation was performed every 90-meters (or 3-arcseconds) along the path to a maximum distance larger than any potential terrain blockage. The maximum distance in this case is about 672 km and is based on the distance at which two points at the tallest point on earth, Mt. Everest, would have line-of-sight blocked by the curvature of the earth, as shown in Figure 28. The maximum line-of-sight angle found along the path represents the overall line-of-sight angle for the heading angle currently being calculated.

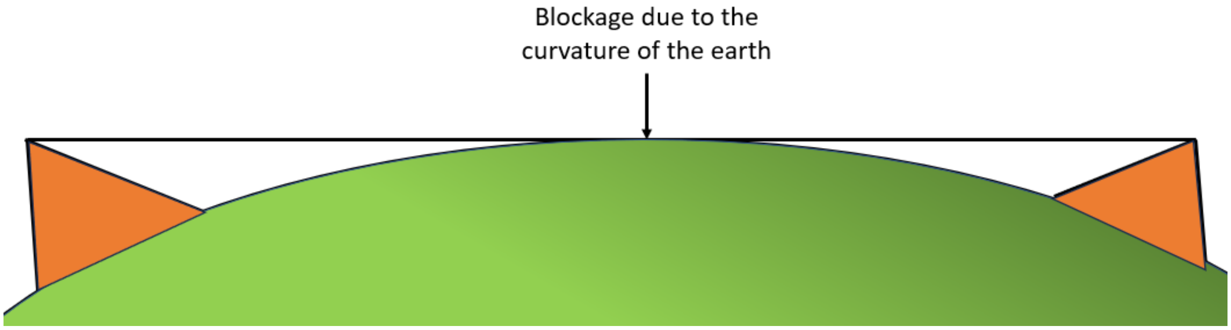

Figure 28: An Illustration of Line-of-Sight Blockage by the Curvature of the Earth.

To improve the accuracy of the line-of-sight calculation, two additional steps were taken to improve the terrain elevation accuracy. The first improvement is higher resolution terrain data, 1/3 arcsecond, is used in the near vicinity of each grid point. This approach is accomplished by loading in 1/3 arcsecond terrain data for a 3x3 block of 1x1 degree terrain tiles centered on the 1x1 degree tile containing the current grid point.

This additional step provides higher accuracy terrain data in the surrounding area of the grid point where the terrain is more likely to block the line-of-sight.

The second improvement for the terrain elevation accuracy of the points along the path included bilinear interpolation on the terrain elevation data. This approach leads to more accurate estimates of the terrain elevation since the points on the path do not normally fall directly on an individual terrain point. Rather, the path typically falls somewhere between terrain points. If no elevation data is available in the 1/3 arcsecond data set the program will fall back to the 3-arcsecond terrain data to obtain the elevation information.

Another improvement made during the generation of the data set involved the chosen floating-point precision of the variables used during the calculation. Using single-precision floating point variables would significantly reduce the generation time of the dataset but would come at a cost of significant errors in the result in some scenarios. Before generating the full dataset, multiple test areas were chosen and the line-of-sight pre-calculation was performed for the 1x1 degree tiles associated with these areas using single and double floating-point precision for comparison. For these test areas the majority of the differences were less than one degree, but some experienced as much as 10-degree differences in value. Due to this large variation, double precision variables were used during the generation of the dataset. This choice led to a significant overall computation time due to the limited number of double-precision compute units on GPUs.

While the calculation was completed using double-precision variables, the resulting values were saved using single-precision floating-point format, to reduce storage size. The generation of the precalculated dataset was performed using CUDA and 24 NVIDIA Tesla V100's housed at the Computational Research Center at the University of North Dakota. The overall dataset consists of about 3TB of uncompressed binary data.

Whenever GPS coverage analysis is performed, this pre-calculated dataset is read from disk and used as a lookup table. Depending on hard drive read speed, this process can be the largest contributor to the runtime of the coverage analysis. Attempts to accelerate the load times of the dataset using file streaming and memory mapping with little observed benefit. To simplify the approach, the program loads each file fully into memory while processing the corresponding area.

GPS Coverage Analysis

The first step of the GPS coverage analysis is to pull the latest GPS TLE orbit prediction, project the satellite constellation to the desired time of analysis, and then convert the satellite location information to a usable format as described above. Then for each of the 3-arcsecond (~90m) grid points in the U.S., the relative geodetic offset of all of the GPS satellites is determined for that grid point so the elevation angle of the GPS satellites may be determined. These calculated elevation angle values are then compared with the corresponding precalculated terrain line-of-sight values; the satellite is considered visible if its elevation angle is above the terrain line-of-sight angle. The total number of satellites that are visible is saved for the current grid point and this process is then repeated for the entire area with the results saved to file in the form of 1x1 degree areas that align with the terrain data.

These visible satellite counts represent the GPS coverage analysis and can be used to generate maps that display areas of coverage, or gaps in coverage, based on a user defined required number of visible GPS satellites. Samples of these results are shown in Figure 29 and Figure 30 where the gaps in coverage, white squares, increase as the required number of visible satellites increases from 5 to 8. These figures are results from an earlier version of the program before improvements were made to the underlying code and the generation process for the precalculated line-of-sight datasets.

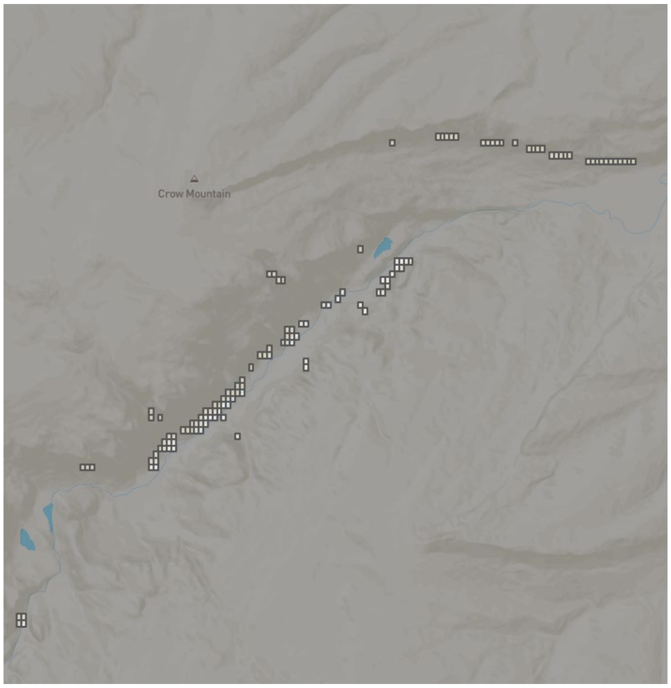

Figure 29: GPS Coverage Analysis with 5 GPS Satellite Minimum for Valley in Wyoming.

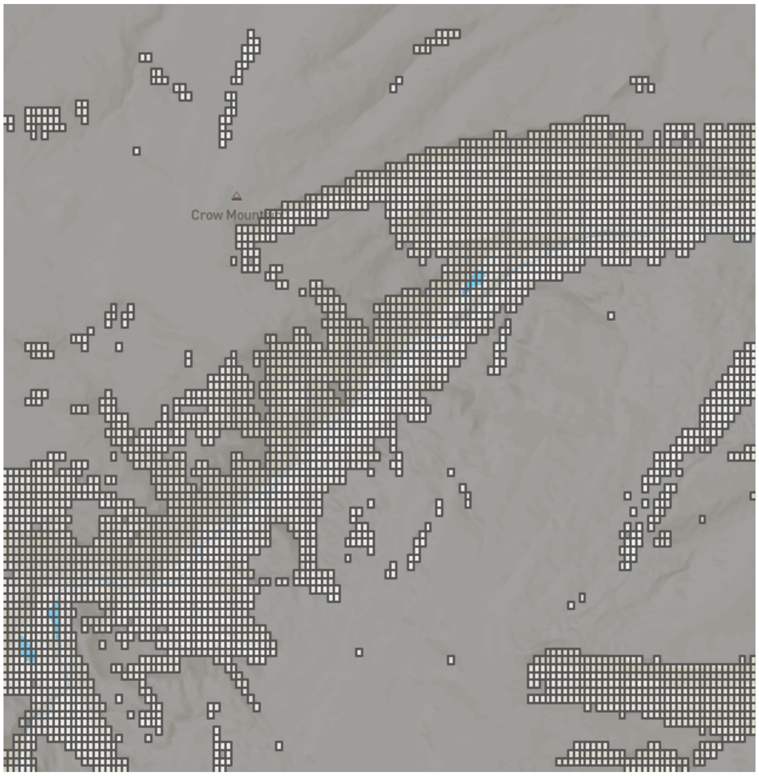

Figure 30: GPS Coverage Analysis with 8 GPS Satellite Minimum for Valley in Wyoming.

The primary usage of the GPS coverage analysis is for the website developed by Botlink, as shown in Figure 31. This website automates the above process and provides an efficient portal to view the latest GPS coverage analysis. As shown in the figure, the user can easily select the required number of visible satellites on the bottom of the screen and the map will update showing the coverage gaps in red for the required number of satellites.

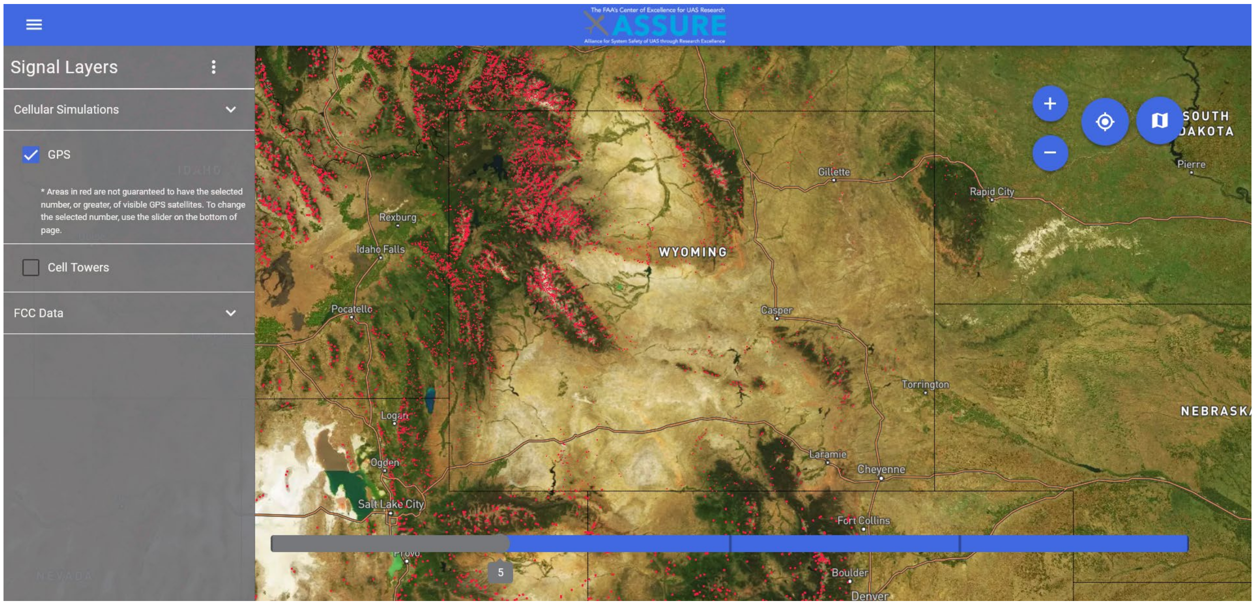

☑ GPS

* Areas in red are not guaranteed to have the selected number, or greater, of visible GPS satellites. To change the selected number, use the slider on the bottom of page.

☐ Cell Towers

Figure 31: Botlink Website GPS Coverage Analysis Interface.

The website developed by Botlink simplified the process of debugging and evaluating the performance of the GPS coverage analysis. The result of this process is presented in the form of two examples of GPS coverage using the latest version of the code and datasets shown below. The first example is shown in Figure 32 which depicts a lake in Washington State with a 5 GPS satellite requirement. In this example, the coverage appears to be worse when near the south facing side of the nearby mountains and cliffs which would indicate operations on the southern side of the lake would potentially have better GPS coverage when compared to the north side of the lake.

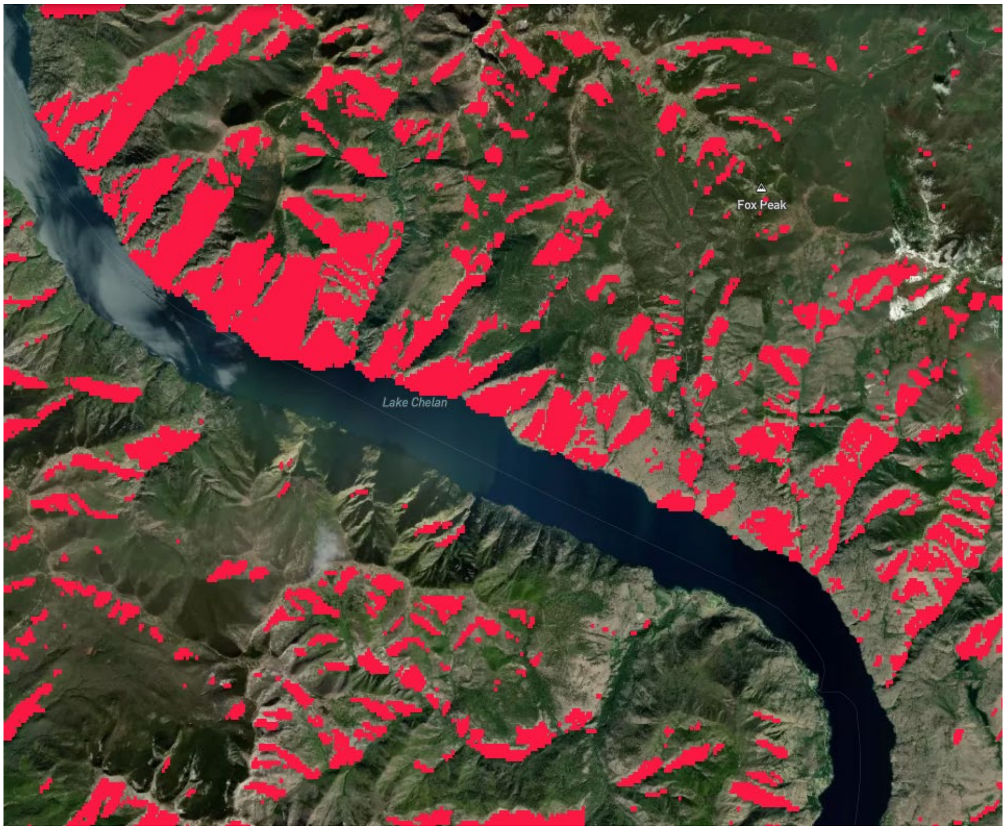

Figure 32: GPS Coverage Analysis for 5 Satellites at a Lake in Washington State.

Another example requiring 5 GPS satellites is located in a mountainous region in Wyoming State as shown in Figure 33. For this region, the coverage again appears to be the worse on the south facing side of the mountains which would indicate that operating near the north facing sides of the mountains could potentially provide better GPS coverage if operations need to be performed in the valleys between the mountains.

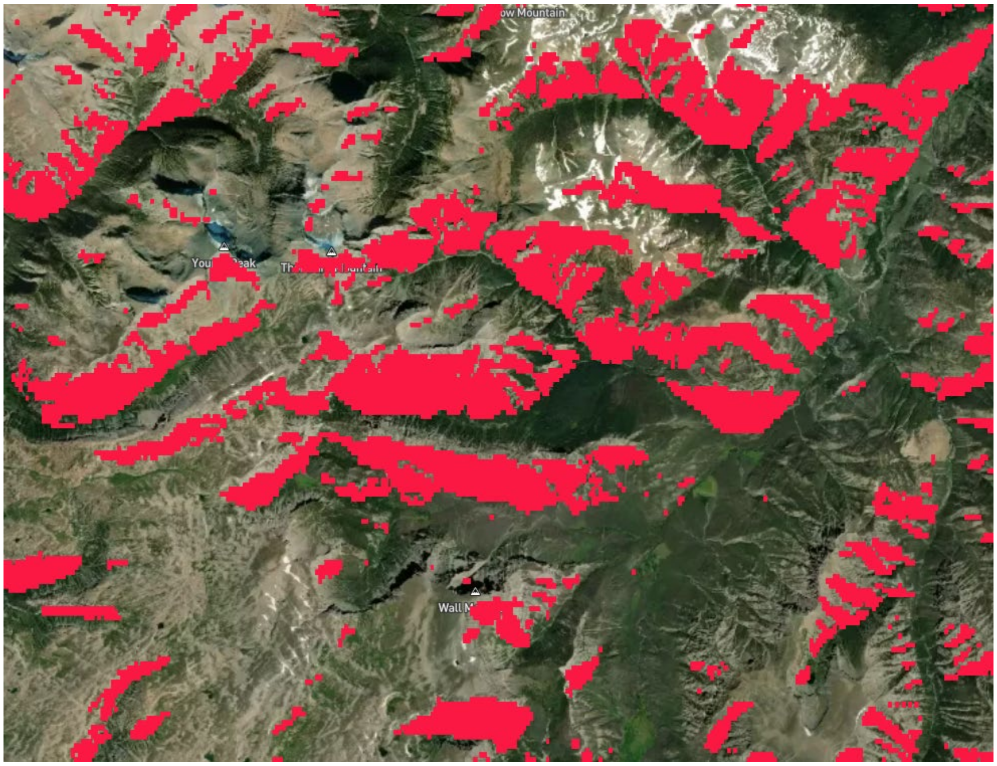

Figure 33: GPS Coverage Analysis for 5 Satellites for a Mountain in Wyoming state.

Reducing Server Runtime

The current version of the program performs the coverage analysis every hour and uses the results for that associated hour. This process is repeated hourly for a total of 24 coverage analyses performed each day. While the approach to calculate the coverage on an hourly basis is sufficient to provide accurate coverage data, the predictability of the GPS constellation suggests that it may be possible to reuse results from one day at a later time when the constellation repeats. Such an approach could significantly reduce the compute requirements of the system.

Performing the analysis every hour incurs an inherent positional error as time passes since the analysis was performed. This error is caused by the reality that GPS satellites do not occupy a geostationary orbit, but instead the constellation orbits the earth approximately every 12 hours. The positional error in meters, and change in angle, over time as observed from the ground, can be found in Table 3. A 30-minute interval results in about a 4.712-degree change in position while a 60-minute update interval results in an error of about 9.282 degrees.

Table 3: GPS Positional Change with Time.

Interval (minutes)	**Position (m)**	**Angle (degrees)**
30	1,664,992	4.712
60	3,301,496	9.282

To reduce the overall server time required to perform the GPS coverage analysis, the feasibility of performing the coverage analysis at a fixed interval for a 24-hour period and then using the results as a lookup dataset for an extended period of time was evaluated. This process works by performing the GPS coverage analysis over a 24-hour period and then using that resulting set of coverage maps as a lookup table where the generated result with the smallest amount of GPS satellite positional error compared to the satellites current positions is used. The estimated positional errors or drift of the satellites over time are shown in Table 4. Using the data for two weeks results in an error of approximately 1-degree in the angle, as observed from the ground. This amount of error is not significant when compared to the amount of positional error from the satellite orbiting the earth, as shown in Table 3. At a period of one month, the positional error rises to approximately 4-degrees, and at a period of 6 months the positional error rises to about 7.7-degrees. At this point, the error compounds with the error of Table 3, which would result in the total error being almost doubled compared to the error associated with performing the analysis every hour. The increase in error is relatively linear and could allow for longer periods of time between regenerating the 24-hour GPS analysis.

Table 4: GPS Positional Change for Out of Data TLE Orbit Data.

Interval (minutes)	**Position (m)**	**Angle (degrees)**
1	37,718	0.107
7	229,537	0.651
14	357,546	1.014
30	767,181	2.175
60	1,427,283	4.042
120	2,060,610	5.825
180	2,725,267	7.684

Due to time constraints, this feature was only analyzed and initially implemented, but has not been fully tested or integrated into the Botlink website. Further work is needed to implement and test this result in practice.

Localization Techniques in GPS Denied Environments

Localization Techniques Classification

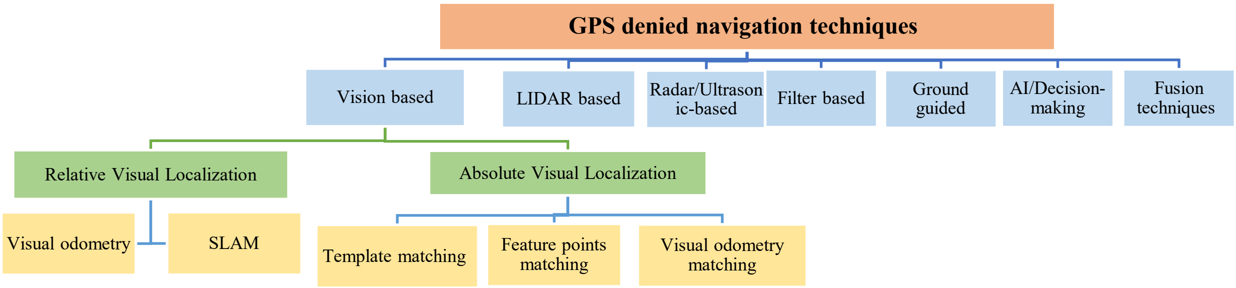

Figure 34: Categorization of All Publications Identified in Terms of their Approach to Navigation in GPS Denied Environments.

1.1.19 LiDAR-Based Techniques

LiDAR technology is increasingly being utilized for UAS localization in environments where GPS is unavailable. This remote sensing method uses laser beams to accurately measure distances and create comprehensive maps in one, two, or three dimensions [14]. Its growing appeal lies in the recent advancements that have significantly improved its range detection capabilities, accuracy, and portability due to reduced size and weight [15]. Particularly beneficial in GPS-denied zones, LiDAR-based methods offer precise, centimeter-level positioning solutions, overcoming the challenges of reliable UAS navigation [16]. A series of research articles have been reviewed to explore various applications of LiDAR in this field.

In [17], the authors developed a system for autonomous navigation of micro air vehicles (MAVs) in GPS-denied environments, focusing on a LiDAR-based system for a quadrotor helicopter. This system, which integrates a high-speed laser scan-matching algorithm, a data fusion filter, in addition to a Simultaneous Localization and Mapping (SLaM) module, enables the quadrotor to autonomously explore and map unstructured and unknown environments. The core of their research is a multilevel sensing and control hierarchy designed to accurately estimate the MAV's position and velocity considering the constraints in payload, computation, and communication on such small vehicles. The effectiveness of this system was demonstrated in various settings, including indoor spaces and urban canyons, during the 2009 International Aerial Robotics Competition. The system, however, encountered challenges in complex 3D environments and featureless settings, where the scan matcher had difficulties in accurately calculating the vehicle's movement. For instance, in the urban canyon experiment, the maximum deviation from the target trajectory was 0.27m, significantly higher than in indoor flights. Additionally, the SLaM and planner modules are designed to operate offboard, requiring frequent communication with the ground station, which poses an additional challenge.

The approach in [18] focuses on navigating large distances in environments where GPS is unavailable, specifically using a system that combines inertial navigation with LiDAR-based localization. The core of this navigation system is the integration of semi-regular updates from LiDAR data with an existing Digital Elevation Model (DEM), alongside an innovative use of an error-state Kalman filter that includes estimations for biases in the Inertial Measurement Unit (IMU). This setup ensures a consistently accurate estimate of the aircraft's state, minimizing the need for extensive computations when consulting the global elevation map. A significant aspect of the system is its ability to match LiDAR scans to specific areas of the DEM, generating a map that highlights the symmetry of the landscape. This process identifies the most likely position of the aircraft, enabling corrections to be applied to the navigational system to ensure accuracy over long distances without GPS input. The study showcases the system's ability to accurately determine an aircraft's location over a journey of 218 kilometers, achieving an impressively low final positional deviation of only 27 meters.

In [19], the authors introduce a novel 3D simulation system for mini-UASs in GPS-denied environments, using a hybrid approach that integrates the Robot Operating System (ROS) with the Unity3D game engine. The system's key innovation is its ability to run real-time multi-UAS navigation and control algorithms, handling large volumes of sensor data. ROS provides a clear software structure and facilitates hardware interaction, while Unity3D offers robust graphics for 3D environment and sensor modeling. The paper also discusses the development of a TCP/IP-based interface between ROS and Unity3D, detailed modeling of environments and UAS sensors (especially LiDAR), and a user-friendly interface for simulation setup and monitoring. The system's efficacy is demonstrated using a forest search scenario with autonomous UASs.

In [20], the study focuses on using LiDAR-based SLaM for drone navigation in GPS-denied environments. The research uses MATLAB simulations to test the drone's navigation capabilities by generating LiDAR data and applying 2D SLaM with pose graph optimization. Key to their approach is analyzing the impact of loop closure threshold and search radius on the optimization process, which affects the drone's trajectory accuracy and mapping. They found that adjusting these parameters can significantly enhance processing speed and trajectory accuracy compared to ground truth. However, the study's limitations include its confinement to 2D data and lack of real-world testing to validate the simulation results, which may affect its practical applicability in complex 3D environments.

The paper [21] introduces an approach for 3D motion planning of Vertical Take-Off and Landing (VTOL) UASs in GPS-denied, unknown forest and cluttered environments. The core of this method involves using LiDAR sensors to detect and map the surrounding environment, creating a dynamic 3D occupancy grid map that the UAS navigates through. The approach combines an online path planning algorithm based on the A* search algorithm with an online trajectory generation method based on maneuver automation techniques. These components work together to generate an obstacle-avoidant path for the UAS. The effectiveness of this integrated LiDAR-based system is demonstrated through both simulations and real flight tests on a UAS equipped with dual LiDAR sensors, highlighting its capability in real-time motion planning and obstacle avoidance in challenging terrains like forests. However, the research does not explore how effectively the proposed method can adjust to unpredicted environmental factors, leaving an evaluation of its adaptability and resilience in variable conditions unaddressed.

In [22], an Adaptive Kalman Filter (AKF) is used to enhance the velocity and position estimation of UASs in environments where GPS signal is either weak or obstructed. The approach integrates data collected from different sensors like LiDAR, GPS, and an Inertial Navigation System (INS). In situations where both LiDAR and GPS data are unavailable, the system relies solely on measurements from the IMU. However, when new data from the LiDAR becomes available, the system's measurement equations are updated to integrate this new information into the Kalman filter process. The key innovation lies in adapting the measurement noise covariance of the AKF based on GPS receiver errors and LiDAR point-cloud matching errors. This adaptation significantly improves the accuracy and reliability of position estimates.

The study in [23] evaluates advanced LiDAR-based 3D SLaM approaches for accurate indoor mapping. Using a simulation framework with ROS and Gazebo, the research compares two distinct methods:

Lightweight and Ground-Optimized LiDAR Odometry and Mapping (LeGO-LOAM) and LiDAR Inertial Odometry via Smoothing and Mapping (LIO-SAM). These methods were tested in varied simulated indoor environments, including empty square rooms, long narrow corridors, and circular rooms, each representing different spatial complexities and clutter levels. The results indicate that LIO-SAM surpasses LeGO-LOAM in accuracy for indoor environments. However, the research is limited to simulations, and real-world implementation of these methods has not been explored in this study.

Despite the promising capabilities of LiDAR in UAS navigation, it is essential to acknowledge its limitations. Challenges arise in adverse weather conditions, like heavy rain or fog, which can impair the LiDAR sensor's performance. Environments with limited line-of-sight, such as dense forests or urban areas with tall structures, also pose significant obstacles. Moreover, the computational demands of processing large volumes of LiDAR data can strain onboard computing resources, leading to potential delays in decision-making and increased energy consumption. Furthermore, the high cost of LiDAR technology remains a barrier to widespread adoption. Addressing these challenges is critical for enhancing the feasibility and efficiency of LiDAR-based UAS localization systems in a variety of operational contexts.

Table 5: A Summary of Pertinent Parameters Associated with Publications that Discuss LiDAR-Based Techniques.

Paper	Hardware	Aircraft	Accuracy	Location	Experiment	Distance
[17]	• Offboard Computer • IMU • LiDAR sensor	Pelican quadrotor helicopter (Micro air-vehicle)	• Maximum trajectory deviation: 0.27 m	Indoor/ Outdoor	Real-world	285 m 745 m 710 m
[18]	• IMU • LiDAR sensor	Bell 206L (LongRanger) helicopter	• Maximum position error: 90.2 m	Outdoor	Real-world	196 km 218 km
[19]	• IMU • Two LiDAR sensors	N/A	• N/A	Outdoor	Simulation	N/A
[20]	• N/A	N/A	• Maximum Root Mean Square Error: 13.75m	N/A	Simulation	N/A
[21]	• IMU • Two LiDAR sensors • Range finder	Quadrotor UAS	• N/A	Outdoor	Real-world	N/A
[22]	• IMU • LiDAR sensor	DJI S1000 octocopter	• Final position drift: 3.42 m	Outdoor	Real-world	405 m
[23]	• IMU • LiDAR sensor	N/A	• Max. Root Mean Square Error: ○ LeGO-LOAM: 1.291 m	Indoor	Simulation	N/A

			○ LIO-SAM: 0.599 m			

1.1.20 Radar/ Ultrasonic-Based Techniques

In environments where GPS signals are not accessible, localization methods like radar-based and ultrasonic-based systems are employed. These systems operate by emitting radio waves or ultrasonic pulses and then measuring the interval between the signal's transmission and its reception. This measurement, combined with known data about the waves' travel speed, allows for the calculation of the time taken for the signals to reach an object and return. This information is then used to accurately estimate the distance to the object, offering an alternative to GPS-based positioning. This summary categorizes recent studies into radar-based and ultrasonic-based techniques, each offering unique solutions to the challenges of GPS-denied navigation.

The studies in [24] and [25] introduce a millimeter wave radar sensor used to navigate indoor environments. This method utilizes the principles of Interferometric Synthetic Aperture Radar (InSAR) and a Frequency-Modulated Continuous Wave (FMCW) scheme combined with millimeter-wave technology, diverging from traditional sensors that falter in poor visibility conditions such as dust, fog, smoke, or flames. The key advantage of this system is its ability to conduct high-resolution 3D mapping and detect moving targets, leveraging the atmospheric penetration capabilities of millimeter waves. While the paper presents a preliminary study, it significantly contributes by developing a software simulator to validate the sensor's functionality. This simulation tool demonstrates the sensor's proficiency in mapping and navigating through challenging, unknown indoor spaces. However, it's important to note that comprehensive evaluation or experimental results of the proposed radar sensor are not provided in this preliminary study. Another work has been conducted in [26], it presents a comprehensive survey of UAS indoor localization techniques, offering insights into various sensor technologies and their respective advantages and challenges. The focus is particularly on the proposal and preliminary testing of an ultrasonic local positioning system, LOCATE-US, developed by the University of Alcalá. This system uses ultrasonic signals from five emitters and processed by a specialized module on a Parrot Bebo 2 drone. The UAS's position was estimated using the Gauss-Newton algorithm, showing low dispersion in both the horizontal and vertical coordinates. Finally, the authors suggest the potential of combining ultrasound with other technologies like cameras or lasers, for more accurate UAS indoor localization in future work.

The paper in [27] introduces an outlier rejection technique to enhance the accuracy and reliability of radar odometry. This technique employs a FMCW radar system equipped with a single transmitting antenna and two receiving antennas positioned along the azimuthal axis. The key innovation is the integration of an odometry-oriented outlier removal algorithm within the Multiple-Target Tracking process, which significantly aids in differentiating between static and moving objects in the viewed scene. This approach is crucial for extracting accurate platform motion information, especially in challenging and cluttered environments. However, the paper does not specify the scenarios or environments in which this method was tested, leaving room for further exploration in its practical application.

The research in [28] presents a GPS-denied navigation technique for small aircraft, using images generated by a Synthetic Aperture Radar (SAR) system. Building upon previous studies, the research uses radar images to calculate range and cross-range positions, employing the Range-Doppler Algorithm (RDA) for efficient image formation. This is particularly suitable for the restricted processing capabilities of small aircraft. The paper introduces an inertial navigation system integrated with radar processing based on an indirect Extended Kalman Filter (EKF), which was tested with both real and simulated flight data. The study demonstrates the practicality and feasibility of SAR-based navigation in GPS-denied environments, showing that navigation errors can be estimated within acceptable limits. The paper also delves into the specifics of SAR image formation, highlighting the applicability and efficiency of the RDA in light aircraft navigation. Another work that uses synthetic aperture radar is [29]. Focusing on integrating SAR with an IMU and an indirect EKF, the study employs an INS and EKF system structure enhanced with radar telemetry for trajectory estimation. In this paper, the core aspect of the research is the evaluation of GPS-denied navigation under various conditions: sensitivity to changes in IMU grades (consumer, tactical, and navigation grade), measurement noise strength from the SAR system, and the geometric relationship between the UAS and targets. The study includes an aircraft navigation and radar simulation that employs Six Degrees of Freedom, validating the covariance of estimation errors through Monte Carlo analysis. The authors address challenges in implementing radar systems for UASs, like computational complexity and image quality, and emphasize the potential of tactical-grade IMUs combined with high-fidelity SAR range measurements in supporting GPS-denied navigation.

In [30], the authors discuss a novel navigation method for small drones using an omnidirectional radar system. The method is designed to estimate the drone's horizontal velocity and height independently from GPS. The radar system, consisting of two circular antenna arrays, is capable of digital beamforming in the receiving mode. The authors also focused on radar-aided positioning in GPS-denied scenarios, addressing the challenges posed by drone platforms' agility and rapid movement. They proposed a 3D motion estimation method that estimates both the radar's height above ground and its horizontal velocity vector. This method involves change-point detection for height estimation, Doppler spectrum analysis for velocity estimation, and a combination of multiple centroid estimates from different steering directions to estimate the drone's course. The authors finally suggest that this system is not only beneficial for navigation but also for coherent radar data processing.

The paper in [31] presents a terrain-referenced navigation algorithm designed to locate and track a UAS in scenarios where GPS is unreliable. The algorithm utilizes a DEM to compare real-time elevation data measured by UAS radar and barometric altimeters against pre-stored terrain profiles. The system pre-processes the DEM to create a database of potential UAS flight profiles, each uniquely identified by a scoring algorithm based on elevation and slope characteristics. During flight, the UAS's measured elevation profile is matched against this database to determine its location. The study algorithm's efficiency is tested through simulations on various terrain sizes and profile lengths, considering practical constraints such as the UAS's ability to fly in all directions with feasible turn rates.

In [32], the authors present a robust localization and tracking system for indoor navigation of drones in environments where GPS is unavailable. The system leverages speaker-generated ultrasonic acoustic signals for estimating the drone's location. It employs a two-stage process; in the first stage, the system uses Frequency Hopping Spread Spectrum with ultrasonic signals for continuous localization of the drone. The Time of Arrival method is employed here, where the system measures the time delay between the transmission of the signal from the drone and its reception at various microphones. This time delay is then used to calculate the distance between the drone and the microphones. In the second stage, the velocity of the drone is estimated by measuring the frequency shift (Doppler shift) of the received signal. These two sets of data (distance and velocity) are then combined using a Kalman filter to provide an estimation of the drone's position. Comprehensive simulations conducted in MATLAB showed that the system can achieve high accuracy in localization, with errors of a few millimeters, significantly outperforming existing systems.

Radar-based techniques, with their ability to perform high-resolution 3D mapping and detect moving targets, offer robust solutions in environments with poor visibility such as smoke or fog. However, these methods often involve complex systems and may require significant computational resources. Ultrasonic-based systems, on the other hand, provide a cost-effective solution with lower computational demands. The precision of ultrasonic systems makes them suitable for indoor navigation where space constraints are a concern. However, these systems may be susceptible to interference from environmental noise and have limitations in range compared to radar-based systems. Both approaches demonstrate significant potential in enhancing reliability and accuracy of navigation in GPS-denied environments, each with its own set of advantages and challenges that need to be considered for specific application scenarios.

Table 6: A Summary of Pertinent Parameters Associated with Publications that Discuss RADAR/Ultrasonic-Based Techniques.

Paper	Hardware	Aircraft	Accuracy	Location	Experiment	Trajectory Distance
[24], [25]	• NA	NA	• 3D geometric resolution: 10–20 cm	Indoor	Simulation	NA
[26]	• Five ultrasonic emitters • FGPA Xilinx Zynq 7000 • ad-hoc ultrasonic acquisition module	Parrot Bebo 2 drone	• Variance: 0.28 m	Indoor	Real-world	NA
[27]	• FMCW 24-GHz SENTIRE Radar • Odroid XU4 embedded CPU • battery for radar • DC-DC converter • IMU	3DR X8+ octocopter	• Max. drift: 10m	Outdoor	Real-world	NA
[28]	• FlexSAR System • NovAtel SPAN CPT7 IMU	NA	• Max. position error: 3m • Max. velocity error: 0.4 m/s	NA	Real-world	51-second GPS-denied flight
[29]	• IMU • SAR system	NA	• Max. position error: 12m	NA	Simulation	NA
[30]	• IMU • Radar system	multi-copter	• Root Mean Square Errors:	Outdoor	Real-world	30 s trajectory

			• Position: 2.6 m • Velocity: 0.32 m/s			
[31]	• Intel(R) Core i7-2620M CPU @ 2.70 GHz • RADAR • Barometric altimeters	NA	• Min. accuracy: ~84%	Outdoor	Simulation	NA
[32]	• ultrasonic speaker • microphones	Quadcopter	• Avg. error: 0.55 cm.	Indoor	Simulation	NA

1.1.21 Filter-Based Techniques

In [33], the authors present a method to estimate a future location and attitude of one UAS platform from observations of a second UAS platform. This estimate of future location and attitude utilizes discrete-time analysis through the definition of a Jacobian that has been extended to a future value rather than the traditional approach of extension of the Jacobian to a previous (past) value. This future extended Jacobian is then used in connection with a Filtering Cramer-Rao Lower Bound (F-CRLB) to provide a lower-bound on future location and attitude. In order to compensate for noise in sensor values, the authors quantify the sensitivity of feedback control parameters to different noise sources in the system. This sensitivity is then combined with the Jacobian Matrix and F-CRLB to provide an accurate estimate of future location and attitude.

The authors of [34] have focused their activities on an attempt to estimate the state of the aircraft at a future moment in time. The team has developed a control approach that is sufficiently efficient that it can be handled entirely on-board a very small, fast and agile aircraft, without input from external sources. The team has successfully demonstrated their approach in a complex environment that is filled with obstacles using an IMU and planar laser range finder. The measurements of the range finder are modified by a Gaussian Particle Filter prior to updating information on current and future UAS state. This approach significantly reduces the amount of data that needs to be processed in order to determine current location and attitude for use in estimating future state.

[35] employs the matrix Lie group of the two-dimensional homogeneous transformation comprised of both translation and rotation. This transformation is employed to account for all nonlinearity associated with a UAS with six degrees of freedom. Sensors in this scenario include IMU and measurements of regional features in the vicinity of the UAS flight. The approach was validated using real-world measurement.

Table 7: A Summary of Pertinent Parameters Associated with Publications that Discuss Filter-Based Techniques.

Paper	Hardware	Aircraft	Accuracy	Environment	Experiments
[33]	• IMU	Two fixed-wing UASs	Max RMSE= 70m	NA	Simulation

[34]	• Hokuyo UTM-30LX laser rangefinder • Microstrain 3DM-GX3-25 IMU • 1.6GHz Intel Atom base flight computer	fixed-wing micro air vehicle	Max. mean velocity error= 0.148 m/s	Indoor	Real-world
[35]	• ADIS16448 IMU • MT9V034 digital image sensor	NA	NA	NA	Simulation

1.1.22 AI/Decision-Making Techniques

AI and decision-making localization techniques have emerged as crucial navigation methods in GPS-denied environments. These advanced techniques leverage artificial intelligence algorithms, including Convolutional Neural Networks (CNNs), Support Vector Machines (SVMs), Recurrent Neural Networks (RNNs), and many other models to analyze data from an array of sensors like cameras and IMUs. By integrating such technologies, UASs can accurately determine their location, orientation, or trajectory in complex environments, ranging from densely built urban areas to cluttered indoor settings. This shift towards AI-driven navigation systems not only enhances the robustness and precision of UAS operations but also paves the way for broader applications in diverse and challenging scenarios.

Many studies have been conducted to implement and improve these methods. In [36], the paper introduces a method for enhancing UAS navigation in GPS-compromised urban environments by delving into end-to-end aerial-road registration. To achieve this, the researchers developed a deep learning framework that leverages an attention-based neural network. Characterized by its dual-branch architecture and shared weights, this network enables the mapping of aerial images and road landmarks into a unified embedding space. A key feature of this model is its Multibranch Attention Module (MBA), which adeptly filters out misleading descriptor matches by concentrating on sparse road features within the images, thus elevating accuracy. Utilizing an extensive dataset of approximately 50,000 paired images of aerial views and road landmarks (created using GIS technology), the approach demonstrates a substantial advancement over current methods in terms of accuracy in rotation angle and x-y translations. In essence, the study's contributions are twofold: firstly, it offers a large-scale dataset for aligned Aerial-Road pairs, encouraging further research in this field; secondly, the unique attention-based neural network architecture significantly enhances accuracy, setting a new benchmark in the domain. Looking ahead, the authors suggest exploring multitask learning in neural networks to simultaneously handle Aerial-Road matching, potentially broadening the applicability and efficiency of their approach.

Another framework is developed in [37], it integrates localization algorithms like SLaM and Visual Odometry (VO) with Partially Observable Markov Decision Processes (POMDPs). The authors have employed a modular system featuring a POMDP solver algorithm implemented in C++, a ROS node facilitating interface and communication with other modules. This integration allows the UAS to make informed decisions in uncertain environments, focusing on safely avoiding obstacles while creating a detailed occupancy map of the environment. The simulation of this framework was done using the Gazebo environment and a 3DR Iris UAS platform.

In [38], the approach utilizes SAR images, comparing newly generated images with pre-obtained reference images to identify navigational errors. The authors employ a CNN structured with a three-channel image configuration that includes the distorted image, the reference image, and their differential image, to pinpoint these errors and precisely determine the UAS flight path. The ResNet architecture forms the core of the neural network, with a modification in its final layer which is substituted by a fully connected layer. Additionally, the research incorporates a transfer learning approach to enhance the network's performance. This method allows the recovery of the true flight path during the synthetic aperture phase. The effectiveness of this neural network-based approach is demonstrated through both simulated and real SAR image data, offering an alternative to GPS-dependent navigation systems in challenging environments. Another study that uses CNN is [39], the authors compare real time imagery captured by the UAS's downward-facing monocular Red-Green-Blue (RGB) camera with pre-existing satellite images using CNN. By matching features and patterns between the UAS current view and the satellite data, the system can estimate the UAS location even in the absence of GPS. It is important to highlight that the success of this method largely depends on the availability of distinct textures in the environment. In regions like suburban areas, where noticeable landmarks are limited, the accuracy of this technique decreases, resulting in a higher margin of error.

In [40], the paper introduces an emergency safe-landing method for UAS in GPS-degraded environments, crucial for Advanced Aerial Mobility and Urban Aerial Mobility. The integrated method combines an INS for dead-reckoning navigation to an identified landing zone, and an Artificial Intelligence-based approach for optical search and object detection. The system employs a 3D depth camera and a fully convolutional neural network to recognize landing features and obstacles, integrated with a Markov Decision Process for collision-free guidance towards the landing zone. The paper presents simulation results demonstrating the system's effectiveness in safely navigating and landing a UAS under challenging conditions.

In their research [41] and [42], Fernando Vanegas and Felipe Gonzalez present a novel approach for navigating UASs in GPS-denied, cluttered environments. They develop a system using a POMDP with an online solver named Adaptive Belief Tree (ABT), tailored for handling uncertainties in sensor data and UAS movement. This system, implemented on a quadcopter equipped with a downward-facing camera and operating on the ROS, recalculates its flight path in real-time to locate targets on the ground whose positions are initially unknown. Through simulations and real flight tests, the study demonstrates the system's efficacy in successfully conducting target finding missions in complex environments without relying on GPS, highlighting the potential of POMDP-based solutions in advanced UAS navigation. In [43], the same authors extended their system to not only locate but also continuously follow a moving ground target. This is achieved through a more sophisticated implementation of the ABT solver, which accounts for the dynamic nature of the target's movements.

The paper [44] presents an innovative approach for enabling a UAS to autonomously land on a moving Unmanned Ground Vehicle (UGV) in environments where GPS is unavailable. The system utilizes a hybrid camera array, combining a fisheye lens camera and a stereo camera, to accurately locate and track the moving UGV. This setup allows for wide Field of View and depth imaging, crucial for precise target location and motion state estimation in dynamic situations. The authors also introduce a novel state estimation algorithm that integrates a CNN model named YOLO v3-tiny for target detection and tracking, alongside a motion compensation algorithm for accurate estimation of the UGV motion. To control the UAS landing maneuver, a nonlinear controller based on the estimated motion state of the UGV is developed.

The system's performance is validated through extensive simulations and real-world experiments, demonstrating its effectiveness and robustness in GPS-denied environments.

In the cited work [45], the researchers present a novel navigation method for UASs operating without GPS. This method uses deep learning to match aerial images taken by the UAS with DEMs, adapting to various lighting and weather conditions by producing several images of each location. The DEMs are created using a detailed per-pixel mapping approach. To evaluate their method's effectiveness, the authors utilized the Inception-ResNet-Fusion architecture, which analyzes the deep terrain features proposed in their study. On the other hand, the paper [46] proposes a method for GPS-denied navigation using low-cost inertial sensors and RNNs. This approach is designed to enhance the reliability of drone navigation when GPS signals are unavailable. The methodology involves training an RNN on a dataset of flight logs, which includes raw sensor measurements from accelerometers, gyroscopes, barometers, and magnetometers, and corresponding state estimates. The network is trained to predict changes in the drone's position and velocity based on these inertial measurements. The system’s performance is validated against a dataset of numerous flight logs, showing its ability to accurately estimate the drone’s position and velocity without GPS data. This is achieved through the network's capacity to learn the error characteristics of low-cost sensors and effectively predict the drone’s motion, showcasing the potential of RNNs in complex navigation tasks under challenging conditions.

Another technique is introduced in [47], the authors approach the navigation of drones in subway and tunnel environments by modeling these structures as network graphs. Drones are viewed as traffic packets in data networks. The navigation within these tunnel networks utilizes router systems at each intersection. These routers are equipped with comprehensive network information and use the Open Shortest Path First protocol for interconnection. To efficiently navigate drones from their source to destination, the routers apply the Dijkstra algorithm, leveraging the available global network information to ascertain the most direct path for each drone.

In their research, the authors of [48] introduce an innovative method for 3-D localization of UAS that leverages 5G cellular networks, which operate independently of GPS systems. The methodology involves formulating the UAS localization problem as an optimization problem that aims to minimize the error in Received Signal Strength Indicator measurements from four adjacent cellular base stations. To address this, the study proposes two machine learning-based approaches: a deep supervised learning technique using Multilayer Perceptron and a reinforcement learning strategy employing Deep Q-Learning (DQN). These approaches are designed to provide near-optimal localization solutions efficiently in real-time dynamic environments. The paper also conducts a comparative analysis of these machine learning techniques against traditional optimization methods, assessing their computational efficiency and effectiveness. Notably, the study suggests that the reinforcement learning approach is more suitable for UASs operating in smaller flight spaces requiring high accuracy, whereas the deep supervised learning approach is recommended for UASs in larger flight spaces due to its lower computational complexity, thereby contributing significantly to the enhancement of UAS localization in urban settings through the use of existing 5G cellular infrastructure.

In the study [49], the researchers developed a novel approach for real-time aerial data collection and mapping without GPS reliance. Their methodology relies on the capabilities of CNNs, particularly the RetinaNet model, to process and analyze visual data captured by UASs. The process begins with the identification and localization of objects of interest and landmarks from the UAS camera, using CNNs to detect pixel coordinates of these elements along with key reference points. This is followed by geometric viewpoint transformation, which projects the identified objects from the UAS perspective view onto an orthogonal map. The research introduces two distinct mapping strategies: Projection from Perspective to Orthogonal based on Reference Objects' Coordinates and Projection from Perspective to Orthogonal based on Reference Objects' Size. These methodologies were validated through outdoor field experiments, emphasizing their effectiveness in creating accurate mappings in environments devoid of GPS data. The approach is primarily dependent on an RGB camera, indicating that its performance might vary with changes in environmental lighting conditions. However, the study successfully demonstrates a significant advancement in UAS-based mapping technologies, highlighting the potential of CNNs in transforming aerial data collection, particularly in GPS-challenged scenarios. On the other hand, the authors of [50] proposed a data-driven solution using Spectrally Normalized Memory Neuron Network (SN-MNN). It leverages rotor revolutions per minute and historical UAS states, predicts the UAS's position, and transforms it into GPS coordinates. This process includes state refinement through an extended Kalman filter-based state fusion. However, it is important to note that despite the SN-MNN advanced capabilities, its complexity may limit is applicability in high-speed, real-time operations.

In [51], an advanced quadrotor navigation method that operates effectively in GPS-challenged and low-light environment is explored. Central to this approach is the use of a Red-Green-Blue-Depth (RGB-D) camera, which is able to identify predefined 3D markers. Significantly, the system incorporates an SVM algorithm for the efficient recognition and classification of these markers. This integration of RGB-D cameras with SVM-based marker identification enables the quadrotor to accurately determine its location and orientation, offering an alternative to conventional GPS navigation systems.

The application of AI and decision-making techniques in UAS localization presents a blend of advantages and limitations. These methods, particularly effective in GPS-denied environments, enhance the autonomy and flexibility of UASs. AI algorithms excel in processing complex sensory data, enabling UASs to navigate through challenging terrains and urban landscapes with precision. The integration of deep learning models like CNNs and RNNs with UAS systems facilitates accurate object detection, mapping, and path planning, even under uncertain conditions. However, these techniques have their constraints. The complexity and computational demands of advanced AI models can be a limiting factor, especially for real-time applications requiring swift processing. Dependence on external environmental factors, such as lighting conditions or the presence of identifiable landmarks, can impact the accuracy of these methods. Furthermore, the effectiveness of AI-based navigation heavily relies on the quality and diversity of the training data, making the systems potentially less reliable in unfamiliar settings. Despite these challenges, the continuous advancements in AI and machine learning promise to mitigate these limitations, paving the way for more robust and versatile UAS navigation solutions.

Table 8: A Summary of Pertinent Parameters Associated with Publications that Discuss AI-Based Techniques.

Paper	Hardware	Aircraft	Accuracy	Location	Experiment	AI-Model
[36]	• Camera	NA	• MAE: • X= 5.2067 • Y= 4.5221	Outdoor	Simulation	GeoCNN + MBA
[37]	• Depth sensor	3DR Iris	• NA	Outdoor	Simulation	POMDP-SLaM

[38]	• Synthetic aperture radar	NA	• MSE < 1	NA	Simulation	Wide ResNet
[39]	• Canon IXUS 125 HS camera	SenseFly eBee	• Error < 50m	Outdoor	Real-world	CNN
[40]	• RealSense • D435i depth camera • IMU	Quadcopter	• NA	Outdoor	Simulation	YOLO v4
[41] [42] [43]	• Camera • IMU • Magnetometer • ultrasonic pressure sensor • barometric pressure sensor	Multi-copter	• Success: 96.25% of the time	Indoor	Real-world	POMDP
[44]	• Binocular Stereo • Camera, Fisheye Lens • Camera • NVIDIA Jetson TX2 • Landmarked UGV	DJI M100	• Error: ~0.5m	Outdoor	Real-world	YOLO v3-tiny
[45]	• Monocular Camera	NA	• Min. Accuracy ~88%	Outdoor	Simulation	CNN
[46]	• IMU ICM-20689 and BMI055, • Magnetometer IST8310, • Barometer MS5611	Quadrotor, Fixed Wing, Standard VTOL, Octorotor, Tiltrotor VTOL, and Hexarotor	• Mean Max Position Error: 85.79m	NA	Simulation	RNN
[47]	• Routers	NA	• NA	Indoor	Simulation	Dijkstra
[48]	• NA	NA	• Deep Learning: 2.6m • Reinforcement	Outdoor	Simulation	Deep Learning (MPL) Reinforcement

			Learning: 0.87m			Learning (DQN)
[49]	• RGB • camera	Parrot Anafi Parrot Bebop 2	• Max. average projection error: 17.18 inch	Outdoor	Real-world	RetinaNet
[50]	• Accelerometer • gyroscope, • barometer • compass	micro-UAS	• Root Mean Square Error: 0.05953 m	Outdoor	Real-world	SN-MNN + EKF
[51]	• ASUS Xtion Pro Live RGB-Depth sensor, Nitrogen6x • Quad-Core ARM Cortex A9 processor.	Quadrotor	• Max lateral error: 2.45 cm • max heading error: 2.89 deg	Indoor	Real-world	SVM

1.1.23 Fusion Techniques

Another method employed for UAS localization in GPS-denied environments is the utilization of fusion techniques. In navigation, fusion techniques involve the integration of data from multiple sensors to enhance accuracy and reliability, particularly in GPS-denied areas where traditional positioning signals are unreliable. These techniques combine measurements from sensors like IMUs, visual sensors (such as cameras), LiDAR, Radar, and more, each contributing unique data about the device's motion and its surroundings. The fusion process employs filtering algorithms like Kalman filters to fuse and process the sensor data, mitigating errors and providing a more accurate estimation of the device's position, orientation, and velocity.

In [52], the authors introduced the All-Source Navigation (ASN) system, developed by BAE Systems Australia. ASN stands out for its adaptability and flexibility; at its core, it makes use of SLaM techniques and can integrate multiple sensors (IMU, camera, height sensor, etc.), offering a plug-and-play navigation solution. When the raw data collected from these sensors is fused in a Kalman filter, it is possible to update the state estimate of the vehicle with less than 4 satellites. This adaptability not only enhances navigational accuracy but also reduces reliance on expensive, high-accuracy IMUs and GPS equipment, making ASN a cost-effective choice. Practical tests conducted on the Kingfisher 2 UAS platform highlight ASN's performance.

The authors in [53] designed and implemented a cost-effective vision-based UAS tailored for GPS-denied navigation in extremely low-light conditions and thermal imaging applications. This UAS leverages onboard sensors, notably a downward-facing optical flow camera, to enable semi-autonomous navigation within GPS-deprived indoor environments. The system's horizontal position is determined through the integration of horizontal velocity data, which, in turn, is computed by fusing inputs from the PX4Flow camera and IMU. Additionally, the vertical position is directly measured using the ultrasonic sensor incorporated within the camera. The authors conducted an indoor flight test in near-complete darkness in order to assess the system's efficacy and potential utility in scenarios requiring precise navigation and thermal imaging capabilities.

Similar to the previous paper, many studies have been conducted to make navigation in low-light conditions more accurate. In [54], the authors proposed a complete platform design and software architecture of a GPS-denied navigation SLaM based technique for MAVs. The system combines measurements of a 3D LiDAR, an altimeter, and a stereo camera to improve the performance of state estimation. This combination is used since optical sensors alone are susceptible to motion blur. The designed platform accounts for the computational resources requirements to meet the Size Weight and Power (SWaP) constraints of the MAV. The performance of the optical sensors has been also addressed in [55], where the authors built a sensor integration system that combines a stereo camera with a rotating sensor-laser range finder to solve the previous systems challenges such as camera's low performance in low illumination environment and the high cost of a 3D range finder. On the other hand, [56] describes the development of a UAS for autonomous tracking and landing on a moving platform in an environment with ultra-low illumination. A customized marker illuminating with infrared LED was secured on the moving platform to be utilized as a landing pad. The UAS installed with a monocular camera with an IR filter was used to track the marker to follow and land on the moving platform. Sensor reading from an onboard LiDAR scanning range finder was fused with a barometer to determine the absolute height relative to the marker and to measure the descent velocity during the landing process.

Some applications usually require high speed navigation, which is why a study has been conducted in [57] to enhance this aspect of navigation. The authors built a quadrotor system that is able to navigate through both indoor and outdoor environments which is mainly used in object detection tasks. As the robot is flying at speeds of more than 18m/s, it constantly senses the environment using a stereo camera, updates the maps and plans a trajectory towards the goal using a laser-based height sensor for state estimation. Another system that focused on the UAS speed was designed in [58]. The study presented a navigation solution that consists of a stereo camera, IMU, and a height sensor fused together to allow autonomous navigation in indoor cluttered environments; in addition to a LiDAR to generate a 3D voxel map. However, the system does not use a global map but instead uses a local mapping technique that generates a point cloud around the current robot location. This point cloud is used to build a 3D voxel map. The results show that the system was able to fly at a speed of 7m/s with a 0.2 m drift in the y-position and a 0.5m in the z-position. Another study that uses velocity estimation is presented in [59], the authors proposed a global optical flow-based velocity estimation of multicopters by fusing measurements from onboard sensors, including a downward-looking monocular camera, an IMU, and a sonar facing downwards. The AirSim-based simulation showed a maximum position error of 0.51m.

In [60], the authors have introduced an autonomous radioactive source localization system using a small aerial robotic platform in GPS denied known and unknown environment. The system relies on radiation detection using a radiation detector, source localization, 3D mapping and finally independent navigation towards the source. Since small aerial robots have limited endurance and due to the need for long dwelling times to allow the radiation counting statistics to provide reliable estimates, the authors developed a method to operate with a minimal number of measurements, resulting in a localization error of 0.31m. [61] presents a SLaM system that remotely calculates the pose and environment map. The proposed system adapts to the sensory configuration of the aerial robot, by integrating different SLaM methods based on vision, laser, and/or inertial measurements using an EKF. To do this, a minimum onboard sensory configuration is supposed to consist of a monocular camera, an IMU, and an altimeter. It allows to improve the results of well-known monocular visual SLaM methods (LSD-SLaM and ORB-SLaM are tested and compared in this work) by solving scale ambiguity and providing additional information to the EKF. A 2D laser sensor can be incorporated to the SLaM system, obtaining a local 2.5D map and a footprint estimation of the robot position that improves the 6D pose estimation through the EKF. [62] is another work that uses Kalman filter, in this case a relative multiplicative extended Kalman filter for estimating the relative state of a multirotor vehicle operating in a GPS-denied environment. The filter fuses data from an inertial measurement unit and altimeter with relative-pose updates from a keyframe-based visual odometry or laser scan-matching algorithm. Because the global position and heading states of the vehicle are unobservable in the absence of global measurements such as GPS, the filter in this article estimates the state with respect to a local frame that is collocated with the odometry keyframe. As a result, the odometry update provides nearly direct measurements of the relative vehicle pose.

The proposed system in [63] uses a sensor combination, which consists of an image sensor and a range sensor only. The main idea behind this system is to investigate whether it is possible to abandon the need for an IMU, which plays the most important role in navigation. However, this sensor combination cannot provide all the information required for conventional guidance, navigation, and control systems. Therefore, the authors also developed an integrated guidance system that requires navigation information obtainable from the sensor combination. This proposed system replaces the body angular rate loop to the look angle rate loop obtained from the image sensor. A numerical simulation has been performed to test the performance of this system which resulted in a maximum tracking error of 5cm.

In [64], the authors present a navigation system that uses the INS, optical flow, and magnetometer for localization of UAS. The magnetometer is used for altitude estimation, whereas the INS and the optical flow are combined for an accurate position and velocity estimate. The proposed approach is based on the extended version of Kalman filter. Experiment findings demonstrate that the suggested technique may greatly minimize navigation position, velocity, and attitude errors when compared to INS-only navigation.

Another system presented in [65] has been designed to access remote sites and collect data of structures and field features following an earthquake or a natural disaster in a GPS-denied environment. The authors proposed a vision and marker-based localization method that uses LiDAR scan data and camera payload integrated with an octo-rotor UAS to reconstruct geometric features of the surrounding environment. After collecting data from sensor combination, the system fuses the information using a Kalman filter algorithm for pose estimation.

The work in [66] proposes a localization methodology based on an improved iterative closest/corresponding point based on point to line metric algorithm for position estimation of a quadrotor UAS in GPS-denied unknown environments. The quadrotor is equipped with a miniature laser range finder as the main onboard sensor.

In the analyzed literature, a common theme emerged where numerous systems utilize teams of UAS. These groups of UASs are primarily engaged in target search operations and environmental exploration tasks. For example, in [67], the authors present a multi-UAS system that can be utilized for a team of UASs to autonomously navigate, search, and detect multiple targets in a cluttered and GPS-denied environment. The multi-UAS system uses a decentralized framework based on Decentralized Partially Observable Markov Decision Processes to formulate the decision-making process considering uncertainties in the environments and sensing. This system was designed for a mission that needs to cooperate efficiently to search and find multiple targets, without knowing possible locations, by sharing limited vital observations through Wi-Fi connection. The system was tested in several cluttered and GPS-denied environments simulated in Gazebo and ROS interface. The environments were populated with different numbers and types of obstacles, several targets, a team of UASs and boundaries.

Another similar work in proposed in [68], the authors designed a framework for a team of UASs to cooperatively explore and find a target in complex GPS-denied environments with obstacles. The team of UASs autonomously navigates and finds the target in a cluttered environment with a known map. The framework is based on a probabilistic Decentralized Partially Observable Markov Decision Processes which accounts for the uncertainties in sensing and the environment. The system is simulated using the ROS and Gazebo. Performance of the system with an increasing number of UASs in several indoor scenarios with obstacles is tested. Results indicate that the proposed multi-UAS system has improvements in terms of time-cost, the proportion of search area surveyed, and successful rates for search and rescue missions.

The paper in [69] aims to give a comprehensive survey on the RF based localization systems with different radio communication technologies and localization mechanisms on UAS positioning. Toward this end, an evaluation framework is first established to evaluate the performance of each system on UAS positioning from different perspectives. Particularly, the Ultra-wideband (UWB) based system with time-based mechanisms is highlighted for UAS positioning under the consideration of the proposed evaluation framework. Finally, an analysis is conducted about the current challenges and the potential research issues in this area to identify the promising directions for future research.

In [70], the work proposes a self-localization approach for tethered drones in GPS-denied environments without using a cable-tension force sensor. The proposed approach uses an extended Kalman filter to estimate the cable-tension force and the three-dimensional position of the drone with respect to a ground platform. The approach uses data reported by the onboard electric motors, accelerometers, gyroscopes, and altimeter (ultrasound sensor), embedded in the commercial-of-the-shelf IMUs. The paper also presents a 4-state state-space model to estimate the drone's 3D location, as well as the cable-tension force. The proposed approach was compared with an existing work that assumes known cable-tension force, and simulation results show that the proposed approach produces estimates with less than 0.3m errors when the actual cable-tension force is greater than 1N.

In conclusion, fusion techniques in GPS-denied environment navigation present a blend of advantages and limitations. On the positive side, they offer enhanced accuracy and reliability in navigation by integrating data from various sensors like IMUs, cameras, LiDAR, RADAR, and others. This multi-sensor approach is adaptable to different scenarios, including low-light and cluttered environments, and is cost-effective as it reduces reliance on expensive GPS and high-accuracy IMUs. Moreover, these techniques, particularly when employing Kalman filters, are effective in mitigating sensor errors and providing precise estimations of position, orientation, and velocity, which is crucial in challenging environments.

However, there are limitations. The effectiveness of these systems heavily depends on the quality and calibration of the sensors used. Inconsistent or inaccurate sensor data can lead to errors in navigation. Additionally, the computational complexity of processing and fusing data from multiple sources can be significant, posing challenges in terms of processing power and real-time application, especially in smaller UASs with limited computing resources. There's also the issue of designing systems that can robustly handle varied and unpredictable environmental conditions, which can significantly impact sensor performance.

A review of 19 papers in this field revealed that 16 of them utilized the IMU in the fusion operation, 13 employed a visible light camera, while 6 incorporated LiDAR and range finders in their sensor combinations. Notably, the position error in these studies ranged from as low as 0.07m to as high as 11m, highlighting the variability in system performance based on sensor choice and integration techniques.

Table 9: A Summary of Pertinent Parameters Associated with Publications that Discuss Fusion-Based Techniques.

Paper	Aircraft	Aircraft specs	Sensors/ Processors	Evaluation metrics	Location
[52]	Kingfisher 2 UAS	• Mass (including payload): 125Kg • Wingspan; 4.13m • Wing area: 2.67 m2 • Max. airspeed: 100 kts • Max. crosswind: 15kts • Max. tailwind: 10kts	• Kontron CP308 board • IMU • Downward-Looking camera • Air data system • Height sensor	• Average position error <10m (peak at 11m) • Mean execution time= 0.39ms	Outdoor
[53]	Quadrotor	• Mass (including thermal camera): 1108g • Propeller size: 9.4x5.0 (inch)	• Main controller board: Teensy 3.1 MCU board • IMU is based on FreeIMU sensor suite • Pololu Mini Maestro Servo Controller board • Thermal camera	• horizontal velocity ±0.2m/s • altitude ±0.15m • heading angle ±0.1 rad	Indoor
[54]	Micro-Aerial Vehicle (MAV)	• 650 mm diameter • 5.5 kg mass	• Downward laser altimeter • IMU • 3-D LiDAR • Intel NUC i7	• Final drift is around 13% of the total traveled distance	Indoor
[55]	Customized quadrotor	• 128cm, tip to tip • Max takeoff weight: 5kg • Payload weight: 2kg	• Stereo camera • Rotating sensor-laser range finder	• Reconstructed range: 30m (building a 3D map)	Indoor/ Outdoor
[56]	Customized quadcopter	--	• Camera • LiDAR • Scanning range finder	• Max x-position error ~ 1m • Max y-position error ~ 1m	Indoor/ Outdoor

			• IMU • Intel NUC with i7 processor	• Max z-position error ~ 3m	
[57]	DJI F450 frame with the DJI E600 propulsion system	--	• Stereo camera • IMU • Laser height sensor • Nodding Hokuyo LiDAR • Intel NUC i7 processor	Max position error ~2m	Indoor/ Outdoor
[58]	DJI F450 + E600		• Cameras • Garmin LiDAR-lite • VectorNav VN-100 IMU • Height sensor • Intel NUC i7 computer • Intel i7-5557U processor	At 7m/s: • Y-position: Max of 0.2m drift • Z-position: Max of 0.5m • X-position: desired and estimate are the same	Indoor/ Outdoor
[59]	DJI Matrice 100 quadcopter	--	• Downward-looking monocular camera • IMU • Sonar facing downwards • NVIDIA Tegra K1's 4-Plus-1 Quad-core ARM Cortex-A15 Processor	Max error of 0.51m	Indoor/ Outdoor
[60]	Small aerial robot	take–off weight: 2.6kg	• Radiation detection system • Pixhawk-autopilot • Intel processor • Visual-inertial sensor • Cesium-137 radiation source	Localization error: 0.31m	Indoor

[61]	Bebop Drone of Parrot Erle-Copter of Erle Robotics	--	• Monocular camera • IMU • Altimeter	RMSE: 103.71cm Mean: 49.82cm	Indoor
[62]	Hexacopter in a Y6 configuration	--	• MEMS IMU • Altimeter • Intel i7 processor • Forward facing asus Xiton Pro Live RGB-D camera	Max error: • Position: 0.0648m • Attitude: 1.6259 degrees • Velocity: 0.1784m/s	--
[63]	--	--	• Image sensor • Range sensor	Max error= 5cm	Indoor
[64]	Mictoaerial vehicle (MAV):DJ 1 2312	--	• Magnetometer (HMC3883L) • Optical flow sensor (PX4FLOW) • IMU (MPU6050)	• Error= 1.8% of the travelled distance • Position error: • X max error ~ 2.25m • Y max error ~ 6m • Z max error ~ 0.65m	Outdoor
[65]	octo-rotor UAS platform	• Payload capacity: 0.8Kg • Vehicle weight with battery: 2.5Kg	• Light detection sensor • LiDAR • High resolution camera • IMU • 1.7GHz ARM Quad-Core 2GB RAM Processor	• Reconstruction of the geometric feature of surrounding environment	Indoor
[66]	Built by the authors	• Four brushless electrical motors and 10 in propellers • 2300 mAH battery • Weight= 1.6Kg • Size= 0.45m x 0.45m	• Hokuyo UTM-30LX miniature laser range finder • IMU • Gumstix embedded computer	• Indoor hovering control experiment: • Horizontal displacement error< ±0.1 m • Altitude error < ±0.2m.	Indoor/ Outdoor

				• Trajectory tracking control experiment (outdoor): • The tracking error < ±0.2m.	
[67]	Small-size quadcopter (multiple)	--	• Downward facing cameras • Multi-orientation range sensors • IMU • Intel® Core™ i7-6700	• Collision rate: max of 44% • Success rate: min 55%	Indoor
[68]	3DR Iris (multiple)	--	• Range laser sensors • Map of the environment • IMU • Downward-facing camera	• Min target detection rate: Independent: 37.5% • Divided: 67.5% • Informed: 82.5%	Indoor
[69]	Custom-built UAS platform	--	• RGB-D camera • 2D LiDAR • Altimeter • IMU	• ~0.25m	Indoor
[70]	--	--	• IMU • Accelerometer • Gyroscope • Altimeter • Cable-tension-force sensor	• Position Error: < 5.075m • Root Mean Square Error: < 0.3m	Indoor/ Outdoor

1.1.24 Ground Guided Techniques

This collection of papers delves into ground-based techniques for UAS navigation in GPS-denied environments. These methods explore various approaches, including triangulation, trilateration, path planning using cellular towers, and cooperative localization, each offering solutions to enable precise and reliable UAS navigation without reliance on satellite-based positioning.

The paper in [71] presents a navigation system for UAS operating in GPS-denied environments. The system leverages a ground-based multi-antenna localization setup, where the UAS, equipped with an aviation transponder (either mode C or S), communicates with these antennas. The ground-based system calculates the UAS's position using triangulation (multilateration) of the time elapsed for responses between the UAS and the antennas. This position information is then relayed back to the UAs via a data telemetry link. The

UAS's autopilot utilizes this information for navigation, similarly to how it would use GPS-based data. The system architecture is specifically designed to enable UAS operation in environments devoid of Global Navigation Satellite Systems like GPS.

In [72], the authors propose a relative navigation method for UASs in GPS-denied environments. This method, utilizing wireless ranging information, constructs three virtual base stations using distance data collected at different time intervals. Remarkably, it requires only one actual ground-based station for calculating the UAS's position. The authors compared their technique to traditional multi-base station wireless positioning methods, which usually have an error margin of over 10cm. This method achieves similar accuracy with the added convenience of requiring just one base station.

The study in [73] presents a two-stage trilateration method for precise, real-time positioning of drones in GPS-denied environments, such as under bridges or indoors, using UWB technology known for its high-ranging accuracy and transmission rate. This technique requires multiple UWB devices: one installed on the UAS and others on ground-based targets. The trilateration method calculates the position by measuring relative distances through signal transmission between these devices, determining the target's position in a fixed coordinate system. This method not only significantly reduces altitude error but also enhances positioning reliability in challenging GPS-denied areas. Additionally, the UAS itself can be used to locate ground users in such environments, offering a robust solution for drone navigation and positioning.

The paper in [74] introduces a path planning method for UASs in GPS-denied environments, using cellular towers as navigation landmarks. The proposed UAS path planner aims to travel optimally from a specific source to a goal location, taking into account the presence of these landmarks. In areas lacking landmarks, the vehicle employs dead reckoning, with the objective of determining a time-optimal path while maintaining covariance within certain bounds. Due to the complexity of solving this as a continuous domain stochastic optimal control problem, the path is discretized into waypoints. The optimal locations of these waypoints are determined using particle swarm optimization, combined with a rabbit-carrot-based path-following technique, to achieve a near-optimal path that meets the specified criteria.

The paper in [75] introduces a cooperative localization technique for UASs in GPS-denied environments, utilizing a ground sensor architecture for guidance. This technique ensures that each UAS remains in constant contact with at least one Unattended Ground Sensor, which acts as a beacon for relative navigation, eliminating the need for dead reckoning. In [76], the authors present an Ultrasonic Beacon System (UBS) for UAS localization and mapping in GPS-denied environments, specifically targeting areas under bridges. The system comprises mobile beacons mounted on UAS's and stationary beacons placed in the surrounding environment, with beacon software monitored on the Ground Control Station. An Extended Kalman Filter algorithm estimates position data using the mobile beacon's position and IMU data. Additionally, the paper describes experiments where autonomous UASs (Pixhawk and Bebop2) equipped with UBS and deep learning were used for structural damage detection, focusing on concrete crack detection.

The work in [77] explores the use of UASs for indoor construction site monitoring in GPS-denied environments. It introduces a method employing fiducial markers (AprilTags) linked to 3D coordinates in Building Information Models for UAS localization. By using cameras onboard UASs to identify their position relative to these tags, the method allows for precise navigation in indoor settings.

The ground-based techniques for UAS navigation in GPS-denied environments, as discussed in these papers, bring forth notable advantages, such as the ability to operate in confined or indoor spaces, under bridges, or in heavily built-up areas where GPS signals are weak or non-existent. The use of UWB technology, cellular towers, ultrasonic beacons, and fiducial markers demonstrates a level of innovation and flexibility in UAS navigation.

However, these techniques also come with certain limitations. The reliance on ground-based infrastructure, such as multiple antennas or beacons, can pose logistical challenges in terms of deployment and maintenance. The accuracy and reliability of these systems can be affected by environmental factors, such as signal interference or physical obstacles, which might impact the communication between UASs and ground sensors. Furthermore, some methods require complex computational algorithms, like Extended Kalman Filters or particle swarm optimization, which could demand significant processing power and potentially limit real-time responsiveness.

Table 10: A Summary of Pertinent Parameters Associated with Publications that Discuss Ground Guiding Techniques.

Paper	Aircraft	Aircraft specs	Hardware	Evaluation metrics	Environment
[71]	Finwing Sabre (controlled by a Pixhawk autopilot)	Finwing Sabre: Weight: 3.12Kg Wingspan: 1.9m	ADS-B transponder, Multiple antennas, Ground control station.	Deviation from the planned trajectory: 60-80m	Outdoor
[72]	--	--	Base station Wireless link	Standard deviation of errors: x-axis: 0.1357m y-axis: 0.1467m z-axis: 0.0669m	Outdoor
[73]	--	--	UWB transmitters	Average position error <1m	Indoor/ Outdoor
[74]	--	--	Landmarks (cellular towers)	x-axis max error: ~30m y-axis max error: 20m	Outdoor
[75]	--	--	UGCs Three UASs/ Two UASs	--	--
[76]	Pixhawk UAS Bebop2 UAS	--	Ultrasonic beacons IMU	Experiment 1: 7 cm latitude, 3.1 cm longitude Experiment 2: error< 17cm	Indoor/ Outdoor
[77]	Parrot Bebop 2	Weight: 500g Flight time ~ 25min Operation range: up to 2Km Video resolution: 14MP	Cameras, tags	Maximum error < 0.5m	Indoor

		Image resolution: 1920x1080 pixels, 30 frames/sec			

1.1.25 Vision-Based Techniques

Vision based techniques encompass the range of sensors intended to perform some combination of camera/visual sensor function in a number of spectrum configurations from purely visual to near-infrared and infrared sensors. As is common in these systems, there may be a combination of methods used to perform localization. The emphasis, however, is on the uniqueness of the proposed solution with respect to vision systems themselves. The primary metric for evaluating vision research besides size, weight and power (which remain relatively small, especially where vision sensors are solely used in localization) is error, especially horizontal, linear error. Altitude can be compensated for by using combinations of IMU and air data sensors. Rotation is useful in understanding the stability and reliability of aircraft, but the ability to track lateral position is the main measurement of success.

a) Visual Odometry (Feature Point and Direct Methods)

Visual Odometry is unique in the categorization of vision-based localization methods. There are two varieties under research, feature-based and direct. The former focuses on selecting features valuable for tracking from frame to frame to establish motion and rotation information. The latter focuses on pixel selection to accomplish the same task and is the newer of the two. While nominally separated in the taxonomy of approaches across relative and absolute visual location, it is also appropriate to compare the two directly which we do in the review of techniques here.

Visual odometry uses a progressive sequence of camera or other visual sensor images to estimate the relative location and rotation of an unmanned aircraft. The direct, or pixel selection method, is the newer of the two. Instead of pulling feature points and tracking those points, pixel changes are tracked from image to image instead, providing motion and rotation information to perform localization.

The technique's advantages include the ability to mount systems in locations that may not be vertically oriented, though most research uses and tests these systems in such a configuration. The technique may also be more suitable to autonomous operations where terrain may vary and very local details might not be mapped with sufficient precision or known. More than one VO solution does use pre-mapping as part of the solution, but this, again, is the nature of vision solutions, especially where they are part of a larger localization package.

The first of the techniques [78] uses monocular vision (single camera) to provide localization. One contribution of this work focuses on the system algorithms and feature database that uses a confidence index to rank and manage the usefulness of feature points, including dropping features where appropriate. However, the primary contribution of the work is flight test validation that includes not only indoor flight test and outdoor flight test, but the transition between the two environments using two different aircraft, a Yamaha Rmax based helicopter (150lb) and micro-copter drone (2lb), demonstrating the flexibility of the system across two different UAS categories. Tracking in results was effective, with horizontal location divergence from GPS position at a maximum of roughly 5-10m and then recovering. Velocity measurement was also reported and tracked a difference within 1 m/s along multiple axes. [79], in research conducted earlier, uses an extended Kalman filter combined with optical flow estimation and also uses the same Rmax platform. However, it simulates the flight and compares the results to real-world flight data from Rmax flights. Results indicate maximum errors within 5m. As an earlier example of the same platform, the results point to the efficacy of their technique, but the real-world flight results of [78] may provide a better indication of both the accuracy and usefulness of similar classes of solutions across multiple aircraft types. A similar flow estimation method was used in [80] and flew indoor tests on a multicopter platform. Results were limited, however, and a comparison between [79] and [80] could not be made.

In [58], the technique implements a hybrid of feature-based and direct methods called "semi-direct visual odometry" (SVO) which uses a variety of depth filtering methods in combination with a stereoscopic camera. Sensor fusion is a core part of the implementation here, utilizing gyroscopic systems in combination with the camera feeding into the SVO solution as a subsystem. Height sensor plus accelerometers accompany the SVO subsystem, feeding into an unscented Kalman filter to produce the localization solution. Finally, LiDAR is used to create mapping, planning, and trajectory generation using graphing methods. The system appears to be robust and mountable on a less than 10lb sUAS flight system. A total solution may not be usable on micro-vehicles but does demonstrate usability on smaller aircraft.

This gives way to [81] which adapts odometry techniques to the specific needs of fixed wing aircraft. In mounting a fixed wing system, the limitations of a vehicle unable to hover and are frequently employed in higher speed, higher endurance, higher altitude missions impose limits on the design of potential odometry systems. Here, relative vision techniques used with a singular monocular camera provides localization without the limitations of shorter-range sensors. A multi-state constraint Kalman Filter is the main component of the fixed-wing system as it is agnostic regarding distance to features. The system employed is a roughly 3lb hand launched aircraft with a 2m wingspan. Flight tests conducted indicate useful navigation but difficulty in straight-line flight, especially over less well-featured terrain with error maximums on the order of 10m. [82] also uses a multi-state constraint filter as an effort to overcome the weaknesses of RGB-D stereo cameras and laser scanners. In simulations using imagery and telemetry acquired from previous flight tests, error using the method accumulated to less than 3% over the flight, 15-20m horizontally.

A number of research efforts focus on indoor navigation at small scale using feature based odometry. While not demonstrating functionality outdoors, another feature matching technique in [83] employs an RGB-D camera that provides stereoscopic light information. The system development was conducted on board a light multicopter flown in indoor environments. The limitation of the stereoscopic system, as with others, remains the limited range of the sensor. The primary contribution of the work, however, is an empirical approach to testing and sampling using the Belief Roadmap algorithm. Overall, multiple sampling methods were tested, and a sampling uncertainty method outperformed others. Practical navigation results indicated a maximum deviation of 19cm. However, this was in indoor environments with limited area. [84] offers a similar test in a limited indoor cluttered environment. The primary contribution involves POMDP tested through simulation using reward functions. In [85], multi-objective functions make the primary contribution with a monocular camera fusion system feeding into the controller. Path planning is accomplished using a potential field. Flight tests validated the adequacy of local control in the Proportional-Integral-Derivative control loop.

[86] poses a unique application of Odometry. Instead of focusing on onboard replacement sensors, here a ground-based system using infrared stereo is used as a landing aid for multiple airborne vehicles, performing a navigation function similar to radio-navigation common to crewed aircraft such as VHF Omnidirectional Range or instrument landing systems. While this component applies directly to the ground-guided portion of the GPS denied localization taxonomy, the odometry focus of this implementation warrants inclusion here. Most notable is the demonstration of guidance to landing for both copter and fixed-wing UAS using arresting cables, very different types of guidance, stages of flight, and even control laws. The landing error for copter flight test remained below 10cm for a 54cm vehicle size. Error for the fixed-wing landing test was below 2m for a touch-down area of four arresting cables spaced 4m apart. [87] presents a similar effort in creating an infrared based approach-and-land system. In this case, visual processing was aimed at actual runway detection and estimation. Errors in flight tests were calculated as Root Mean Square (RMS) values. Given the angular nature of the navigation solution, these values decreased appropriately with proximity to the runway.

Drawing a contrast with previous approaches, [88] attempts to use a prebuilt map to create a basis for pixel matching and alignment with known features and edge detection. For an area of roughly 100x50m, the error remained usually within 2m.

In summary, Visual Odometry is one of the more promising GPS-denied solutions. As with other research, it remains at its best when combined with multiple methods in the taxonomy within the size, weight, power constraints of the platform. As discussed, the faster, higher nature of fixed-wing flight and missions may limit the usefulness of stereoscopic sensors, especially at higher altitudes. But monocular implementations may be sufficient. And the development and interest in ground-based odometry solutions demonstrates that not all localization need be contained and limited to airborne systems that reduce useful mission load. As always, validation in flight is most useful in determining the maturity and readiness of a system for deployment and/or commercialization. Regardless, several solutions have demonstrated that visual odometry is effective and useful for a variety of platforms and environments.

Table 11: A Summary of Pertinent Parameters Associated with Publications that Discuss Techniques Focused Exclusively on Visual Odometry.

Paper	Method	Hardware	Aircraft	Accuracy	Location	Experiments	SWaP
[78]	Visual Odometry	Monocular Vision	Rmax Helicopter/Micro-drone	5-10m transient	Outdoor/ Indoor	Flight Test, Real World	Mounted on 2lb vehicle as well as 150lb
[79]	Visual Odometry	Monocular Vision	Rmax Helicopter	< 5m	Outdoor	Flight Test, Real World	Mounted on 160lb vehicle

[80]	Visual Odometry	Monocular Vision + Ultrasonic Sensor	Small Multicopter	n/a	Indoor	Flight Test, Real World	Small UAS
[58]	Visual Odometry	Stereoscopic camera	Small Multicopter	~1m	Indoor	Flight Test, Real World	Small UAS

Table 12: A Summary of Pertinent Parameters Associated with Publications that Discuss Techniques that Combine Visual Odometry with a Collection of other Approaches.

Paper	Method	Hardware	Aircraft	Accuracy	Location	Experiments	SWaP
[81]	Visual Odometry	Monocular Camera + Jetson TX2	Strix StratoSurfer Fixed-Wing	Max ~0.02m location	Outdoor	Flight Test, Real World	~3lb
[82]	Visual Odometry + Multistate Constraint Filter	Monocular Camera	Small Fixed-Wing	<3%, 15-20m	n/a	Simulation	n/a
[83]	Visual Odometry + Belief Space Mapping	Stereo Camera (RGB-D)	Micro Multicopter	0.19m	Indoor	Flight Test, Real World	Micro Air Vehicle
[84]	Visual Odometry + POMDP	Monocular Camera	Small Multicopter	n/a	n/a	Simulation	n/a
[85]	Visual Odometry	Monocular Camera	Small Multicopter	Control response adequate	Indoor	Flight Test, Real World	Small Multicopter
[86]	Visual Odometry + Ground Based	Ground-Based Hardware	Small Multicopter + Small Fixed Wing	< 0.1m Copter, <2m Fixed Wing	Outdoor	Flight Test, Real World	Small Aircraft, Ground Systems
[87]	Visual Odometry + Ground Based	Ground-Based Hardware (FLIR)	Small Fixed Wing	<1m (FLIR)	Outdoor	Flight Test, Real World	Small Aircraft, Ground Systems

[88]	Visual Odometry	Monocular Camera	Small Multicopter	<2m	Outdoor	Flight Test, Real World	Small Multicopter

b. SLaM

Simultaneous location and mapping, or SLaM, is a mature technology that has been employed successfully in automobile navigation since 2005 and the Grand DARPA Challenge [89]. SLaM is about the buildout of localization while simultaneously creating a map of the environment. A variety of techniques will follow the type of sensor used whether laser (LiDAR) or visual in the case of vision-SLaM. This map-building process is integral to the method and informs the advantages and drawbacks to the technique. This process is also in contrast to visual odometry which focuses on the change of image to acquire the pose of the camera and therefore the vehicle.

A straightforward example of vision SLaM can be seen in [90]. An indoor multicopter platform is used with a monocular camera in concert with the SLaM algorithm. In indoor flight tests, the linear performance was effective. In an earlier flight test, linear error reached less than 0.5m. The error in rotation was significant, however. Earlier map drift caused the full loss of the map in rotation. The addition of a correction step mostly eliminated the issue and RMS error was reduced to less than 5cm. [91] reported a similar monocular setup with an extended Kalman filter. As part of the design, however, the flexibility of vision systems is demonstrated by this project's inclusion of a visual odometry algorithm coupled with the SLaM solution. In outdoor test flights, error was held to the centimeter level. [92] performed similarly undergoing indoor tests with a micro UAS and single camera. The source mentions the use of a laser rangefinder in larger multicopter aircraft but left off this implementation. Error remained small, well within centimeter distances. Also employing monocular vision and a laser rangefinder was [17]. However, beyond development of the system and visual depiction of mapping results from the laser, no data on accuracy was provided. [93] is an older research effort exploring SLaM with a monocular camera. In indoor testing, the error recorded was nevertheless, less than 2m demonstrating the efficacy of the technique in early practical tests.

One interesting system developed in [94], sought to focus on Martian exploration for former bodies of water. A combination of visual odometry and SLaM techniques plus POMDP mentioned earlier, the research's contribution is primarily toward mapping techniques for survey, ultimately off Earth. The techniques, however, provide navigation capability and, in concert with a monocular visual-inertial state estimator, resulted in simulation test with RMS error greater than 20m. Authors report calibration issues contributing to the results.

In an effort to tackle the problem of higher altitude air navigation, [95] uses a combination of VO and SLaM methods. As an earlier example of the research, a heavier more performant helicopter was used that included PC-104 architecture. As with other SLaM solutions, the vision system is monocular. In part, because of the expected operational altitude, stereo vision would have been of limited use, given the narrow onboard mounting separation. Horizontal error in one axis during flight tests that incorporated all solutions was less than 5m.

The changing nature of outdoor environment, especially where lighting constantly changes, [96] sought to use an algorithm processing low resolution images within a SLaM structure. While the platform is ground-only, the effort to mitigate a combination of environmental factors is a notable contribution. As before, visual odometry is coupled with the SLaM system. There is not extensive error data as the research was intended to demonstrate viability of the technique.

Of the two, SLaM and visual odometry, SLaM is the more mature technology. However, as demonstrated here, the two are not incompatible. Multiple sources show the use of both. The focus of the research here, however, is the SLaM technique, at least in concert with the physical systems. It is also notable that there is a lack of laser mapping such as the LiDAR systems found in autonomous automobile development. Where there are lasers used, it is primarily in either indoor, small volume settings or at very low altitudes given the range limitations of lasers. It is evident that SLaM's clear weaknesses: less effective in transient environments with no opportunity to map and the inability to deal with non-static objects such as ground vehicles or people, indicates a reliance on secondary systems. This is likely a contributor to the fact that visual odometry is also used often in these solutions.

Table 13: A Summary of Pertinent Parameters Associated with Publications that Discuss Techniques Focused Exclusively on SLaM.

Paper	Method	Hardware	Aircraft	Accuracy	Environment	Experiments	SWaP
[90]	Vision SLaM	Monocular Camera	Micro Multicopter	<5cm	Indoor	Flight Test, Real World	Small Multicopter
[91]	Vision SLaM	Optical Flow Camera	Small Multicopter	<0.1m	Outdoor	Flight Test, Real World	Small Multicopter
[92]	Vision SLaM	Monocular Camera + Laser Rangefinder	Micro Multicopter	<0.1m	Indoor	Flight Test, Real World	Small Multicopter
[17]	Laser SLaM	Laser Rangefinder	Small Multicopter	n/a	n/a	n/a	Small Multicopter

Table 14: A Summary of Pertinent Parameters Associated with Publications that Discuss Techniques that Combine SLaM with a Collection of other Approaches.

Paper	Method	Hardware	Aircraft	Accuracy	Environment	Experiments	SWaP
[93]	Vision SLaM	Monocular Camera	n/a	<2m	Indoor	Ground Test	Small Aircraft

[94]	Vision SLaM + POMDP	Monocular Camera	Small Multicopter (Martian)	>20m	Outdoor	Simulation	Small Multicopter (Martian)
[95]	Vision SLaM + Visual Odometry	Monocular Camera	Helicopter	<5m	Outdoor	Flight Test, Real World	Helicopter
[96]	Vision SLaM + Visual Odometry	Monocular Camera	Ground Vehicle	b.a	Outdoor	Ground Test, Real World	Ground Vehicle

c. Template Matching

Template matching involves image processing methods that use datasets to evaluate feature alignments. Given a known dataset, vision sensors can be used to align an aircraft's relative position and rotation relative to that dataset. There are advantages and drawbacks to this approach, but a handful of research projects have used the technique.

In [97], the authors use another ground-based landing system similar to [86] and [87]. Here the calibration process includes selecting reference points and matching pre-calibrated imagery taken by IR cameras to the current state of the vehicle. Accuracy in this case (noting that this is angular and so precision increases with proximity to the runway as in instrument landing systems) produced error two within tens of centimeters. [98], in an effort to enable mountainous terrain navigation, used parallax occlusion visual data to match against other imagery, namely drainage patterns. The concept of the work and its contribution are that on-board sensors would produce a product like the latter type of image and localize by comparison to the rugged terrain dataset. This was demonstrated in computation simulation of these images but was not integrated into an aircraft or simulated as an aircraft. The technique warrants further investigation, possibly as part of an evaluation of multiple techniques most suitable to rugged terrain navigation and the various challenges surrounding mountain flight. In [99] a hybrid approach to be integrated into a helicopter was proposed to build maps. The process, from hybrid feature extraction in an initial map creation to generating a more efficient follow-up, works as a system design not yet implemented. In a unique contribution, [100] creates a dataset called "denseUAV" using densely sampled imagery dedicated to UAS navigation. Of interest, these images were collected at 80m, 90m, and 100m above ground to account for the change in perspective downward looking vision sensors would get with altitude change. Coupled with this was a baseline model adapted to take advantage of the dataset. As a demonstration of the methodology, the techniques showed a potential contribution to a systematic use of dataset generation for navigation.

The limitations of template matching are self-descriptive. There must be robust datasets suitable for air navigation. This is difficult because ground features can change dramatically depending on the altitude of the aircraft attempting localization and navigation. This is mitigated by increasing the dataset to account for multiple altitudes worth of information. In any case, this describes a brute force attempt at localization except in known small areas. UAS transiting an area would be much more likely to stumble on terrain and features not found or at least not found along the precise flight plan.

Table 15: A Summary of Pertinent Parameters Associated with Publications that Discuss Techniques that Combine Template Matching with a Collection of other Approaches.

Paper	Method	Hardware	Aircraft	Accuracy	Environment	Experiments	SWaP
[97]	Template Matching	NIR Camera, Ground Equipment	Small Fixed Wing	<1m	Outdoor	Flight Test, Real World	Small Fixed Wing, Ground Equipment
[98]	Template Matching	n/a	n/a	n/a	n/a	Simulation	n/a
[99]	Template Matching + Hybrid Feature Extraction	Monocular Camera	n/a	n/a	n/a	n/a	n/a
[100]	Template Matching + Dataset Creation	Camera (unspecified)	n/a	n/a	Outdoor	Simulation	n/a

d. Feature Points Matching

Visual odometry methods frequently involve feature matching methods. The works discussed here are best categorized as dedicated primarily to feature matching rather than having such methods as part of a larger solution or are treated in isolation from a larger system. [101], for example, emphasizes the feature matching methods directly while still performing simulation and indoor flight test. The contribution to a navigation solution is the claim that as few as four feature points are sufficient for operation. Position error, indeed, remained below 0.5m. In [102], this method was used to create a control loop to system servos for navigation using feature points. The flight platform was a small, nearly micro, UAS. In flight test, the error was tested usually down to the centimeter level over a minute of flight time. The research in [103] performed feature points comparison using Google Map data. Applying the method returned confidence levels of correspondence. In subsequent flight test, the maximum trajectory error appears to be less than 10m. The authors regard this as a successful demonstration of the method given the limitations of the dataset. Gimbal stabilization and thermal cameras are expected improvements. Finally, [104] looks at front-camera image collection for the dataset and then performs feature matching. Simulations conducted indicate that the solution could lead to simultaneous operation in a SLaM-like system.

Table 16: A Summary of Pertinent Parameters Associated with Publications that Discuss Techniques that Combine Feature Points Matching with a Collection of other Approaches.

Paper	Method	Hardware	Aircraft	Accuracy	Environment	Experiments	SWaP
[101]	Feature Points Matching	Monocular Camera	Small Multicopter	<0.1m	Indoor	Flight Test, Real World	Small Multicopter
[102]	Feature Points Matching + Servo Control Loop	Monocular Camera	Micro Multicopter	<0.1m	Indoor	Flight Test, Real World	Micro Multicopter
[103]	Feature Points Matching + Commercial Dataset	Monocular Camera	Small Multicopter	<10m	Outdoor	Flight Test, Real World	Small Multicopter
[104]	Feature Points Matching	Monocular Camera + Augmented Reality	Ground Vehicle	n/a	Indoor	n/a	Ground Vehicle

The upshot of feature points research as a category is that it is a potential avenue for further refinement of algorithms and methodology. As with template matching, preexisting data is required for localization, at least to start. There are interesting potential avenues to pursue such as refinement application of existing datasets as in [103]. The more robust areas of investigation appear to be, on the whole, in visual odometry or in some mixture of methods.

This is a theme across all vision methods. The definition and boundary between the methods is fluid and not strictly limited. A VO solution can certainly feed into a SLaM system. Monocular or binocular vision hardware can couple with multistep control systems to improve the solution. One of the key points of vision methods is that the physical equipment can be lightweight and less demanding on even smaller UAS. There is opportunity for image processing techniques to employ CPU or GPU intensive solutions and that could impose power and weight costs, but continued improvements in mobile processing, especially in ARM, shows that such limitations will decrease over time. The takeaway appears to be that outdoor tests demonstrate the viability or at least the proximity of a solution to wider use. Interest appears to be high in the visual odometry arena and, alone or coupled with other techniques, marks a need for further research in this area.

References

[1] RTCA, "Minimum Aviation System Performance Standards for C2 Link Systems Supporting Operations of Unmanned Aircraft Systems in U.S. Airspace," SC-228, 2021.

[2] Federal Communications Commission, "Mobile LTE Coverage Map," United States Federal Communications Commission, [Online]. Available: https://www.fcc.gov/BroadbandData/MobileMaps/mobile-map. [Accessed 15 May 2021].

[3] Geospatial Management Office, U.S. Department of Homeland Security, "Homeland Infrastructure Foundation-Level Data Open Data," [Online]. Available: https://hifld-geoplatform.opendata.arcgis.com/. [Accessed 29 December 2023].

[4] Unwired Labs, "The world's largest Open Database of Cell Towers," Unwired Labs, [Online]. Available: https://opencellid.org/. [Accessed 29 December 2023].

[5] US Cellular, "U.S. Cellular Tower Locator," [Online]. Available: https://www.uscellular.com/tower-locator. [Accessed 29 December 2023].

[6] CellMapper Serviced Limited, "Cell Mapper," [Online]. Available: https://www.cellmapper.net/Index. [Accessed 29 December 2023].

[7] "AntennaSearch," [Online]. Available: https://www.antennasearch.com/. [Accessed 29 December 2023].

[8] J. Magliacane, "SPLAT! Because the world isn't flat!," 2021. [Online]. Available: https://www.qsl.net/kd2bd/splat.html. [Accessed 29 December 2023].

[9] United States Geological Survey, [Online]. Available: https://apps.nationalmap.gov/downloader/. [Accessed 29 December 2023].

[10] United States Geological Survey, [Online]. Available: https://earthexplorer.usgs.gov/. [Accessed 29 December 2023].

[11] Combined Force Space Component Command , SAIC, [Online]. Available: https://www.space-track.org/. [Accessed 29 December 2023].

[12] T. S. Kelso, "CelesTrak," [Online]. Available: https://celestrak.org/. [Accessed 29 December 2023].

[13] B. Rhodes. [Online]. Available: https://rhodesmill.org/skyfield/. [Accessed 29 December 2023].

[14] S. Hening, C. A. Ippolito, K. S. Krishnakumar , V. Stepanyan and M. Teodorescu, "3D LiDAR SLAM Integration with GPS/INS for UAVs in Urban GPS-Degraded Environments," in *AIAA Information Systems-AIAA Infotech@ Aerospace*, 2017.

[15] T. Raj, . F. H. Hashim, A. B. Huddin, M. F. Ibrahim and A. Hussain, " A Survey on LiDAR Scanning Mechanisms," *Electronics,* vol. 9, no. 5, p. 741, 2020.

[16] B. Yang and A. Yang, "A Survey on Radio Frequency Based Precise Localisation Technology for UAV in GPS-Denied Environment," *Journal of Intelligent & Robotic Systems,* vol. 103, pp. 1-30, 2021.

[17] A. Bachrach, S. Prentice, R. He and N. Roy, "RANGE-Robust autonomous navigation in GPS-denied environments," *Journal of Field Robotics,* vol. 28, no. 5, pp. 644-666, 2011.

[18] G. Hemann, S. Singh and M. Kaess, "Long-range GPS-denied aerial inertial navigation with LIDAR localization," in *IEEE/RSJ International Conference on Intelligent Robots and Systems (IROS)*, Daejeon, Korea, 2016.

[19] W. Meng, Y. Hu, J. Lin, F. Lin and R. Teo, "ROS+unity: An efficient high-fidelity 3D multi-UAV navigation and control simulator in GPS-denied environments," in *41st annual conference of the IEEE industiral electronics society*, Yokohama, Japan, 2015.

[20] J. Ho, S. Phang and H. Mun, "2-D UAV navigation solution with LIDAR sensor under GPS-denied environment," in *15th international engineering and computing research conference*, Subang Jaya, Malaysia, 2021.

[21] F. Liao, S. Lai, Y. Hu, J. Cui, J. L. Wang, R. Teo and F. Lin, "3D motion planning for UAVs in GPS-denied unknown forest environment," in *2016 IEEE Intelligent Vehicles Symposium (IV)*, Gothenburg, Sweden, 2016.

[22] S. Hening, C. Ippolito, K. Krishnakumar, V. Stepanyan and M. Teodorescu, "3D LiDAR SLAM integration with GPS/INS for UAVs in urban GPS-degraded environments," in *AIAA SciTech Forum*, Grapevine, TX, 2017.

[23] T. H. Chan, H. Hesse and S. G. Ho, "LiDAR-based 3D SLAM for indoor mapping," in *7th International Conference on Control, Automation, and Robotics (ICCAR)*, Singapore, 2021.

[24] A. F. Scannapieco, A. Renga and A. Moccia, "Preliminary Study of a Millimeter Wave FMCW InSAR for UAS Indoor Navigation," *Sensors,* vol. 15, no. 2, 2015.

[25] A. F. Scannapieco, A. Renga and A. Moccia, "Compact millimeter wave FMCW InSAR for UAS indoor navigation," in *IEEE Metrology for Aerospace (MetroAeroSpace)*, Benevento, Italy, 2015.

[26] M. C. Perez, D. Gualda, J. de Vicente, J. M. Villadangos and J. Urena, "Review of UAV positioning in indoor environments and new proposal based on US measurements," in *CEUR Workshop*, 2019.

[27] A. F. Scannapieco, M. D. Graziano, G. Fasano and A. Renga, "Improving radar-based mini-UAS navigation in complex environments with outlier rejection," in *AIAA SciTech Forum*, San Diego, California, 2019.

[28] C. Lindstrom, R. Christensen, J. Gunther and S. Jenkins, "GPS-Denied Navigation Aided by Synthetic Aperture RADAR Using the Range-Doppler Algorithm," *Journal of the Institute of Navigation,* vol. 69, no. 3, 2022.

[29] C. Lindstrom, R. Christensen and J. Gunther, "An Investigation of GPS-Denied Navigation Using Airborne RADAR Telemetry," in *2020 IEEE/ION Position, Location and Navigation Symposium (PLANS)*, Portland, OR, 2020.

[30] K. T. J. Klein, F. Uysal, M. C. Cuenca, M. P. G. Otten and J. J. M. de Wit, "RADAR-Aided Navigation System for Small Drones in GPS-Denied Environments," in *IEEE RADAR Conference (RadarConf21)*, Atlanta, GA, 2021.

[31] O. Eroglu and G. Yilmaz, "A novel fast and accurate algorithm for Terrain Referenced UAV localzation," in *International Conference on Unmanned Aircraft Systems (ICUAS)*, Atlanta, GA, 2013.

[32] A. Famili and J. M. J. Park, "Rolatin: Robust localization and tracking for indoor navigation of drones," in *IEEE Wireless Communications and Networking Conference (WCNC)*, Seoul, Korea, 2020.

[33] H. Bai and C. N. Taylor, "Future Uncertainty-Based Control for Relative Navigation in GPS-Denied Environments," *IEEE Transactions on Aerospace and Electronic Systems,* vol. 56, no. 5, pp. 3491-3501, 2020.

[34] A. Bry, A. Bachrach and N. Roy, "State estimation for aggressive flight in GPS-denied environments using onboard sensing," in *IEEE International Conference on Robotics and Automation*, Saint Paul, MN, 2012.

[35] H. A. Hashim, "GPS-denied Navigation: Attitude, Position, Linear Velocity, and Gravity Estimation with Nonlinear Stochastic Observer," in *American Control Conference (ACC)*, New Orleans, LA, 2021.

[36] T. Wang, Y. Zhao, J. Wang, A. K. Somani and C. Sun, "Attention-Based Road Registration for GPS-Denied UAS Navigation," *IEEE Transactions on Neural Networks and Learning Systems,* vol. 32, no. 4, pp. 1788-1800, 2021.

[37] F. Vanegas, K. J. Gaston and J. G. F. Roberts, "A Framework for UAV Navigation and Exploration in GPS-Denied Environments," in *IEEE Aerospace Conference*, Big Sky, MT, 2019.

[38] T. White, J. Wheeler, C. Lindstrom, R. Christensen and K. R. Moon, "GPS-Denied Navigation Using SAR Images and Neural Networks," in *IEEE International Conference on Acoustics, Speech and Signal Processing (ICASSP)*, Toronto, ON, Canada, 2021.

[39] H. Goforth and S. Lucey, "GPS-Denied UAV Localization using Pre-existing Satellite Imagery," in *International Conference on Robotics and Automation (ICRA)*, Montreal, QC, Canada, 2019.

[40] B. Xia, I. Mantegh and W. Xie, "Integrated Emergency Self-Landing Method for Autonomous UAS in Urban Aerial Mobility," in *21st International Conference on Control, Automation and Systems (ICCAS)*, Jeju, Korea, 2021.

[41] F. Vanegas and F. Gonzalez, "Enabling UAV Navigation with Sensor and Environmental Uncertainty in Cluttered and GPS-Denied Environments," *Sensors,* vol. 16, no. 5, 2016.

[42] F. Vanegas and F. Gonzales, "Uncertainty based online planning for UAV target finding in cluttered and GPS-denied environments," in *IEEE Aerospace Conference*, Big Sky, MT, 2016.

[43] F. Vanegas, D. Campbell, M. Eich and F. Gonzalez, "UAV based target finding and tracking in GPS-Denied and cluttered environments," in *IEEE/RSJ International Conference on Intelligent Robots and Systems (IROS)*, Daejeon, Korea, 2016.

[44] T. Yang, Q. Ren, F. Zhang, B. Xie, H. Ren, J. Li and Y. Zhang, "Hybrid Camera Array-Based UAV Auto-Landing on Moving UGV in GPS-Denied Environment," *Remote Sensing,* vol. 10, no. 11, 2018.

[45] T. Wang and A. K. Somani, "Aerial-DEM geolocalization for GPS-denied UAS navigation," *Machine Vision and Applications,* vol. 31, no. 1, p. 3, 2020.

[46] A. AbdulMajuid, O. Mohamady, M. Draz and G. El-bayoumi, "GPS-Denied Navigation Using Low-Cost Inertial Sensors and Recurrent Neural Networks," *arXiv:2109.04831,* 2021.

[47] A. Mirzaeinia, J. Shahmoradi, P. Roghanchi and M. Hassanalian, "Autonomous Routing and Power Management of Drones in GPS-Denied Environments through Dikjstra Algorithm," in *AIAA Propulsion and Energy 2019 Forum*, Indianapolis, IN, 2019.

[48] G. Afifi and Y. Gadallah, "Autonomous 3-D UAV Localization Using Cellular Networks: Deep Supervised Learning Versus Reinforcement Learning Approaches," *IEEE Access,* vol. 9, pp. 155234-155248, 2021.

[49] Y. Pi, D. Nath and A. H. Bezhadan, "Deep Neural Networks for Drone View Localization and Mapping in GPS_Denied Environments," in *37th CIB W78 Conference*, Sao Paulo, Brazil, 2020.

[50] N. Rao, S. Sundaram and V. Raghavendra, "Computationally Light Spectrally Normalized Memory Neuron Network based Estimator for GPS-Denied Operation of Micro UAV," in *9th International Conference on Control, Decision and Information Technologies (CoDIT)*, Rome, Italy, 2023.

[51] A. R. Vetrella, A. Savvaris, G. Fasano and D. Accardo, "RGB-D camera-based quadrotor navigation in GPS-denied and low light environments using known 3D markers," in *International Conference on Unmanned Aircraft Systems (ICUAS)*, Denver, CO, 2015.

[52] P. Williams and M. Crump, "All-Source Navigation for Enhancing UAV Operations in GPS-Denied Environments," in *28th International Congress of the Aeronautical Sciences (ICAS)*, Brisbane, Australia, 2012.

[53] C. Liu, J. Nash and S. Prior, "A low-cost vision-based unmanned aerial system for extremely low-light GPS-denied navigation and thermal imaging," *International Journal of Mechanical, Aerospace, Industrial, Mechatronic and Manufacturing Engineering,* vol. 9, no. 10, pp. 1750-1757, 2015.

[54] H. Lu, H. Shen, B. Tian, X. Zhang, Z. Yang and Q. Zong, "Flight in GPS-denied environment: Autonomous navigation system for micro-aerial vehicle'," *Aerospace Science and Technology,* vol. 124, p. 107521, 2022.

[55] H. Qin, Y. Bi, K. Z. Y. Ang, K. Wang, J. Li, M. Lan, M. Shan and F. Lin, "A stereo and rotating laser framework for UAV navigation in GPS denied environment," in *IECON 2016 - 42nd Annual Conference of the IEEE Industrial Electronics Society*, Florence, Italy, 2016.

[56] X. Chen, S. K. Phang and B. M. Chen, "System integration of a vision-guided UAV for autonomous tracking on moving platform in low illumination condition," in *ION 2017 Pacific PNT Meeting*, Honolulu, HI, 2018.

[57] K. Mohta, K. Sun, S. Liu, M. Watterson, B. Pfrommer, J. Svacha, Y. Mulgaonkar, C. J. Taylor and V. Kumar, "Experiments in Fast, Autonomous, GPS-Denied Quadrotor Flight," in *2018 IEEE International Conference on Robotics and Automation (ICRA)*, Brisbane, QLD, Australia, 2018.

[58] K. Mohta, M. Watterson, Y. Mulgaonkar, S. Liu, C. Qu, A. Makineni, K. Saulnier, K. Sun, A. Zhu, J. Delmerico, K. Karydis, N. Atanasov, G. Loianno, D. Scaramuzza, K. Daniilidis, C. J. Taylor and V. Kumar, "Fast, autonomous flight in GPS-denied and cluttered environments," *Journal of Field Robotics,* vol. 35, no. 1, pp. 101-120, 2017.

[59] H. Deng, U. Arif, K. Yang, Z. Xi, Q. Quan and K. Cai, "Global optical flow-based estimation of velocity for multicopters using monocular vision in GPS-denied environments," *Optik,* vol. 219, 2020.

[60] F. Mascarich, T. Wilson, C. Papachristos and K. Alexis, "Radiation Source Localization in GPS-Denied Environments Using Aerial Robots," in *IEEE International Conference on Robotics and Automation (ICRA)*, Brisbane, QLD, Australia, 2018.

[61] E. Lopez, S. Garcia, R. Barea, L. Bergasa, E. J. Molinos, R. Arroyo, E. Romera and S. Pardo, "A Multi-Sensorial Simultaneous Localization and Mapping (SLAM) System for Low-Cost Micro Aerial Vehicles in GPS-Denied Environments," *Sensors,* vol. 17, no. 4, p. 802, 2017.

[62] D. P. Koch, D. O. Wheeler, R. W. Beard, T. W. McLain and K. M. Brink, "Relative multiplicative extended Kalman filter for observable GPS-denied navigation," *The International Journal of Robotics Research,* vol. 39, no. 9, 2020.

[63] J. Hong, C. Ryoo, H. Shin and A. Tsourdos, "Integrated Guidance, Navigation, and Control System for a UAV in a GPS Denied Environment," in *15th International Conference on Informatics in Control, Automation and Robotics*, Porto, Portugal, 2018.

[64] C. Shen, Z. Bai, H. Cao, K. Xu, C. Wang, H. Zhang, D. Wang, J. Tang and J. Liu, "Optical Flow Sensor/INS/Magnetometer Integrated Navigation System for MAV in GPS-Denied Environment," *Journal of Sensors,* vol. 2016, 2016.

[65] M. Hirose, Y. Xiao, Z. Zuo, V. R. Kamat, D. Zekkos and J. Lynch, "Implementation of UAV localization methods for a mobile post-earthquake monitoring system," in *IEEE Workshop on Environmental, Eneregy, and Structural Monitoring Systems (EESMS)*, Trento, Italy, 2015.

[66] Y. Song, B. Xian, Y. Zhang, X. Jiang and X. Zhang, "Towards autonomous control of quadrotor unmanned aerial vehicles in a GPS-denied urban area via laser ranger finder," *Optik,* vol. 126, no. 23, pp. 3877-3882, 2015.

[67] X. Zhu, F. Vanegas and F. Gonzalez, "Decentralised Multi-UAV Cooperative Searching Multi-Target in Cluttered and GPS-Denied Environments," in *IEEE Aerospace Conference (AERO)*, Big Sky, MT, 2022.

[68] X. Zhu, F. Vanegas, F. Gonzalez and C. Sanderson, "A Multi-UAV System for Exploration and Target Finding in Cluttered and GPS-Denied Environments," in *International Conference on Unmanned Aircraft Systems (ICUAS)*, Athens, Greece, 2021.

[69] W. Youn, H. Ko, H. Choi, I. Choi, J. Baek and H. Myung, "Collision-free Autonomous Navigation of A Small UAV Using Low-cost Sensors in GPS-denied Environments," *International Journal of Control, Automation and Systems,* vol. 19, pp. 953-968, 2021.

[70] A. Al-Radaideh and L. Sun, "Self-localization of tethered drones without a cable force sensor in GPS-denied environments," *MDPI: Drones,* vol. 5, no. 4, 2021.

[71] C. Lum, H. Rotta, R. Patel, H. Kuni, T. Patana-anake, J. Longhurst and K. Chen, "UAS Operation and Navigation in GPS-Denied Environments Using Multilateration of Aviation Transponders," in *AIAA SciTech Forum*, San Diego, CA, 2019.

[72] M. Li, S. Weng, G. Song, N. Wang and Y. Zhang, "A Relative Navigation Method Based on Wireless Ranging for UAV in GPS Denied Environment," in *International Conference on Electrical, Communication, and Computer Engineering*, Istanbul, Turkey, 2020.

[73] Y. Chen, H. Liew, J. Chao and R. Wu, "Decimeter-Accuracy Positioning for Drones Using Two-Stage Trilateration in a GPS-Denied Environment," *IEEE Internet of Things Journal,* vol. 10, no. 9, pp. 8319-8326, 2023.

[74] S. Singh and P. B. Sujit, "Landmarks based path planning for UAVs in GPS-denied areas," *IFAC-PapersOnLine,* vol. 49, no. 1, pp. 396-400, 2016.

[75] S. G. Manyam, S. Rathinam, S. Darbha, D. Casbeer, Y. Cao and P. Chandler, "GPS Denied UAV Routing with Communication Constraints," *Journal of Intelligent Robot Systems,* vol. 84, no. 1, pp. 691-703, 2016.

[76] D. Kang and Y. Cha, "Autonomous UAVs for Structural Health Monitoring Using Deep Learning and an Ultrasonic Beacon System with Geo-Tagging," *Computer-Aided Civil and Infrastructure Engineering,* vol. 33, pp. 885-902, 2018.

[77] M. Nahangi, A. Heins, B. McCabe and A. Schoellig, "Automated Localization of UAVs in GPS-Denied Indoor Construction Environments Using Fiducial Markers," in *35th International Symposium on Automation and Robotics in Construction (ISARC)*, Berlin, Germany, 2018.

[78] G. Chowdhary, E. N. Johnson, D. Magree, A. Wu and A. Shein, "GPS-denied indoor and outdoor monocular vision aided navigation and control of unmanned aircraft," *Journal of field robotics,* vol. 30, no. 3, pp. 415-438, 2013.

[79] Y. Watanabe, P. Fabiani and G. Le Besnerais, "Simultaneous visual target tracking and navigation in a GPS-denied environment," in *International Conference on Advanced Robotics*, Munich, Germany, 2009.

[80] C. Aasish, E. Ranjitha, U. Razeen Ridhwan, S. Bharath Raj and L. Angelin Jemi, "Navigation of UAV without GPS," in *International Conference on Robotics, Automation, Control and Embedded Systems (RACE)*, Chennai, India, 2015.

[81] G. Ellingson, K. Brink and T. McLain, "Relative navigation of fixed-wing aircraft in GPS-denied environments," *NAVIGATION: Journal of the Institute of Navigation,* vol. 67, no. 2, pp. 255-273, 2020.

[82] G. Ellingson, K. Bring and T. McLain, "Relative visual-inertial odometry for fixed-wing aircraft in GPS-denied environments," in *IEEE/ION Position, Location and Navigation Symposium (PLANS)*, Monterey, CA, 2018.

[83] A. Bachrach, S. Prentice, R. He, P. Henry, A. S. Guang, M. Krainin, D. Maturana, D. Fox and N. Roy, "Estimation, planning, and mapping for autonomous flight using an RGB-D camera in GPS-denied environments," *The International Journal of Robotics Research,* vol. 31, no. 11, 2012.

[84] F. Vanegas Alvarez, J. Roberts and F. Gonzalez, "UAV tracking of mobile target in occluded, cluttered and GPS-denied environments," in *39th IEEE Aerospace Conference*, 2018.

[85] T. T. Mac, C. Copot, R. De Keyser and C. M. Ionexcu, "he development of an autonomous navigation system with optimal control of an UAV in partly unknown indoor environment," *Mechatronics,* vol. 49, pp. 187-196, 2018.

[86] W. Kong, D. Zhang, X. Wang, Z. Xian and J. Zhang, "Autonomous landing of an UAV with a ground-based actuated infrared stereo vision system," in *2013 IEEE/RSJ INternational Conference on Intelligent Robots and Systems*, Tokyo, Japan, 2014.

[87] L. Zhang, Z. Zhai, H. L. and P. Wen, "Infrared-inertial navigation for commercial aircraft precision landing in low visibility and gps-denied environments," *Sensors,* vol. 19, no. 2, 2019.

[88] J. Unicomb, L. Dantanarayana, J. Arukgoda, R. Ranasinghe, G. Dissanayake and T. Furukawa, "Distance function based 6dof localization for unmanned aerial vehicles in gps denied environments," in *IEEE/RSJ International Conference on Intelligent Robots and Systems (IROS)*, Vancouver, BC, Canada, 2017.

[89] S. Thrun, M. Montemerlo, H. Dahlkamp, D. Stavens, A. Aron, J. Diebel, P. Fong, J. Gale, M. Halpenny, G. Hoffmann, K. Lau, C. Oakley, M. Palatucci, V. Pratt, P. Stang, S. Strohband, C. Dupont, L. Jendrossek, C. Koelen, C. Markey and et.al., "Stanley: The robot that won the DARPA Grand Challenge," *Journal of Field Robotics,* vol. 23, no. 9, pp. 661-692, 2006.

[90] S. Weiss, D. Scaramuzza and R. Seigwart, "Monocular-SLAM–based navigation for autonomous micro helicopters in GPS-denied environments," *Journal of Field Robotics,* vol. 28, no. 6, pp. 854-874, 2011.

[91] D. Scaramuza, M. C. Achtelik, L. Doitsidis, F. Friedrich, E. Kosmatopoulos, A. Martinelli, M. Achtelik, M. Chli, S. Chatzichristofis, L. Kneip, D. Gurdan, L. Heng, G. Lee, S. Lynen, M. Pollefeys, A. Renzaglia, R. Seigwart and e. al, "Vision-controlled micro flying robots: from system design to autonomous navigation and mapping in GPS-denied environments," *IEEE Robotics and Automation Magazine,* vol. 21, no. 3, pp. 26-40, 2014.

[92] X. Zhang, B. Xian, B. Zhao and Y. Zhang, "Autonomous flight control of a nano quadrotor helicopter in a GPS-denied environment using on-board vision," *IEEE Transactions on Industrial Electronics,* vol. 62, no. 10, pp. 6392-6403, 2015.

[93] J. Langelaan and S. Rock, " Passive GPS-free navigation for small UAVs," in *IEEE Aerospace Conference*, Big Sky, MT, 2005.

[94] A. D. Singh and F. Vanegas Alvarez, "Simulating gps-denied autonomous uav navigation for detection of surface water bodies," in *International Conference on Unmanned Aircraft Systems (ICUAS)*, Athens, Greece, 2020.

[95] F. Caballero, L. Merino, J. Ferruz and A. Ollero, "Vision-based odometry and SLAM for medium and high altitude flying UAVs," *Journal of Intelligent and Robotic Systems,* vol. 54, pp. 137-161, 2009.

[96] M. Milford and A. George, "Featureless visual processing for SLAM in changing outdoor environments," *Field and Service Robotics,* vol. 92, pp. 569-583, 2013.

[97] T. Yang, G. Li, J. Li, Y. Zhang, X. Zhang, Z. Zhang and Z. Li, "A ground-based near infrared camera array system for UAV auto-landing in GPS-denied environment," *Sensors,* vol. 19, no. 9, 2016.

[98] T. Wang, K. Celik and A. K. Somani, "Meta-image navigation augmenters for GPS denied mountain navigation of small UAS," in *Airborne Intelligence, Surveillance, Reconnaissance (ISR) Systems and Applications XI*, Baltimore, MD, 2014.

[99] S. Rady, A. A. Kandil and E. Badreddin, "A hybrid localization approach for uav in gps denied areas," in *IEEE/SICE International Symposium on System Integration (SII)*, Kyoto, Japan, 2011.

[100] M. Dai, E. Zheng, Z. Feng, J. Zhuang and W. Yang, "Vision-Based UAV Localization System in Denial Environments," *arXiv:2201.09201,* 2023.

[101] R. Mebarki, V. Lippiello and B. Siciliano, "Nonlinear visual control of unmanned aerial vehicles in GPS-denied environments," *IEEE Transactions on Robotics,* vol. 31, no. 4, pp. 1004-1017, 2015.

[102] H. Xie, K. H. Low and Z. He, "Adaptive visual servoing of unmanned aerial vehicles in GPS-denied environments," *IEEE/ASME Transactions on Mechatronics,* vol. 22, no. 6, pp. 2554-2563, 2017.

[103] M. Shan, F. Wang, F. Lin, Z. Gao, T. Z. Tang and B. Chen, "Google map aided visual navigation for UAVs in GPS-denied environment," in *IEEE International Conference on Robotics and Biomimetics (ROBIO)*, Zhuhai, China, 2015.

[104] S. Rajeev, Q. Wan, K. Yau, K. Panetta and S. Agaian, "Augmented reality-based vision-aid indoor navigation system in GPS denied environment," in *Mobile Multimedia/Image Processing, Security, and Applications*, Baltimore, MD, 2019.

[105] Federal Communications Commission, "Universal Licensing System," [Online]. Available: https://wireless2.fcc.gov/UlsApp/UlsSearch/frequenciesCell.jsp?licKey=11497&channelBlock=A. [Accessed 29 December 2023].